The LC3B FRET biosensor monitors the modes of action of ATG4B during autophagy in living cells

Elif Begüm Gökerküçük[1], Angélique Cheron[1], Marc Tramier[1,*], Giulia Bertolin[1,2,*].

[1] Univ Rennes, CNRS, IGDR (Institute of Genetics and Development of Rennes), UMR 6290, F-35000 Rennes, France

[2] Lead contact

[*] Correspondence and requests for materials should be addressed to G.B. (giulia.bertolin@univ-rennes1.fr; Tel: +330223237516) or to M.T. (marc.tramier@univ-rennes1.fr; Tel: +330223235487).

Abstract

Although several mechanisms of autophagy have been dissected in the last decade, following this pathway in real time remains challenging. Among the early events leading to autophagy activation, the ATG4B protease primes the key autophagy player LC3B. Given the lack of reporters to follow this event in living cells, we developed a Förster's Resonance Energy Transfer (FRET) biosensor responding to the priming of LC3B by ATG4B. The biosensor was generated by flanking LC3B within a pH-resistant donor-acceptor FRET pair, Aquamarine/tdLanYFP. We here showed that the biosensor has a dual readout. First, FRET indicates the priming of LC3B by ATG4B and the resolution of the FRET image allows to characterize the spatial heterogeneity of the priming activity. Second, quantifying the number of Aquamarine-LC3B puncta determines the degree of autophagy activation. We then showed that there are small pools of unprimed LC3B upon *ATG4B* downregulation, and that the priming of the biosensor is completely abolished in *ATG4B* knockout cells. The lack of priming can be rescued with the wild-type ATG4B or with the partially active W142A mutant, but not with the catalytically dead C74S mutant. Last, we screened for commercially-available ATG4B inhibitors, and we illustrated their differential mode of action by implementing a spatially-resolved, broad-to-sensitive analysis pipeline combining FRET and the quantification of autophagic puncta. Therefore, the LC3B FRET biosensor paves the way for a highly-

31 quantitative monitoring of the ATG4B activity in living cells and in real time, with

32 unprecedented spatiotemporal resolution.

33

34 Keywords: autophagy, LC3B, ATG4B, FRET/FLIM, biosensor

Introduction

36 Conserved in all eukaryotic cells, macroautophagy/autophagy is the lysosome-mediated degradation and

37 recycling of the intracellular components [1]. Autophagy is triggered as a survival response in paradigms such

38 as starvation, pathogen infection or DNA damage, and it contributes to cellular differentiation, immunity,

39 aging and cell death [2–4]. In mammals, autophagy starts at sites of endoplasmic reticulum (ER) enriched for

40 phosphatidylinositol 3-phosphate [PI(3)P]. On these subdomains, a double-membrane structure termed

41 phagophore forms [5]. As the phagophore elongates into a crescent-shaped structure, it engulfs bulk or

42 selective cargoes and then closes into a double-membrane vesicle, the autophagosome. The fusion of

43 autophagosomes with lysosomes results in the degradation of the sequestered cargo by the lysosomal acid

44 hydrolases.

45 A series of AuTophaGy-related (ATG) proteins regulate the autophagic pathway [6]. Among them, a

46 special attention is given to the ATG8 family, which are the key proteins found on autophagosomal

47 membranes at all stages of the pathway. ATG8 proteins are ubiquitin-like adaptor proteins involved in

48 autophagosome formation, biogenesis and cargo selection [7–9]. In mammals, ATG8 proteins belong to two

49 subfamilies, the MAP1LC3/LC3 (microtubule-associated protein 1 light chain 3) and GABARAP (gamma-

50 aminobutyric acid [GABA] type A receptor-associated protein) [10,11]. A total of seven genes - *LC3A*, *LC3B*,

51 *LC3B2*, *LC3C*, *GABARAP*, *GABARAPL1* and *GABARAPL2* - code for the LC3 and GABARAP subfamilies

52 in humans [10]. LC3/GABARAPs are found as inactive pro- forms upon translation, and are activated by the

53 ATG4 family of cysteine proteases [12,13]. In humans, four members of the ATG4 family (ATG4A, B, C and

54 D) are responsible for this activation step, which is to proteolytically cleave the C-terminus of pro-

55 LC3/GABARAP proteins and convert them into the so-called form-I. This crucial cleavage is known as "pro-

56 LC3/GABARAP priming", and it is essential to expose a specific glycine residue required for the lipidation

57 of the cytosolic LC3/GABARAP-I proteins to the phosphatidylethanolamine (PE) head groups of the forming

58 phagophores. This is achieved after a series of reactions that involves the E1-like enzyme ATG7, the E2-like

59 enzyme ATG3 and the E3-like complex ATG12–ATG5-ATG16L1 [12,14–16]. The PE-conjugated

60 LC3/GABARAP proteins are then called LC3/GABARAP-II, and function in membrane tethering,

61 hemifusion, autophagosome formation and cargo recruitment [17–20]. Once the phagophore is fully closed,

62 LC3/GABARAP-II proteins are removed from the outer surface of the phagophore membrane by ATG4s,

63 through the hydrolysis of the link between PE and LC3/GABARAP [12]. Although the importance of this

64 second round of cleavage activity (referred as deconjugation hereafter) by ATG4 was shown to be important

65 for the normal progression of autophagy in yeast [21–23], recent studies in human cells suggest the existence

66 of autophagy-independent roles for the deconjugation activity of ATG4s [24,25]. Therefore, the relevance of

67 ATG4-mediated deconjugation for the progression and completion of autophagy in models other than yeast

68 still requires further investigation [21–26].

69 Autophagy plays an essential role to maintain cellular homeostasis, and its dysfunction has been

70 implicated in many pathological conditions such as neurodegenerative diseases, cancer, inflammation,

71 muscular and hearth disorders [27]. As a consequence, therapeutic options to modulate autophagy emerged as

72 promising strategies for the treatment of these complex pathologies [28]. In this light, targeting ATG4s to

73 inhibit autophagy in its early stages has a significant potential to completely block autophagy [29]. However,

74 currently available compounds targeting ATG4 activity show poor specificity and/or efficacy [30]. In addition,

75 there is a lack of dedicated probes that can be used in living cells to monitor ATG4 activity during autophagy

76 progression. Overall, this creates a bottleneck for the identification of ATG4 inhibitors with improved

77 properties. For these reasons, we developed a Förster's Resonance Energy Transfer (FRET) biosensor, named

78 the LC3B biosensor, to simultaneously monitor: 1) the priming of LC3B by ATG4 and 2) the accumulation

79 of LC3B on the autophagic membranes.

80   The FRET phenomenon is a non-radiative energy transfer between a donor and an acceptor pair of

81   fluorophores. FRET can occur when the emission spectrum of the donor fluorophore partially overlaps with

82   the excitation spectrum of the acceptor, and this only when the two fluorescent moieties are in close proximity

83   (less than 10 nm apart) [31]. This phenomenon can be used to monitor many different cellular events including

84   the exploration of protein-protein interactions, the changes in conformation of proteins, and the up- or

85   downregulation of signaling pathways [32,33]. With the recent advances, FRET quantification by fluorescence

86   lifetime imaging microscopy (FLIM) became a very useful method to study molecular activities in living cells

87   [34].

88   In this study, we present the LC3B biosensor as a superior probe that can be used in living cells to

89   monitor the activation – LC3B priming by ATG4 – and progression – LC3B accumulation on the autophagic

90   membranes – of autophagy, in real time and with high spatial resolution. We show that the biosensor

91   recapitulates the main features of the endogenous LC3B protein in terms of forming puncta-shaped structures,

92   of ATG4B-dependent cleavage, and of its colocalization with lysosomal proteins upon autophagy induction

93   and/or lysosomal inhibition. We also show that the biosensor can report on the changes in proLC3B priming,

94   and this in an ATG4B-dependent manner. Using *ATG4* knockout cells, we demonstrate that the absence of

95   ATG4B maximizes the FRET response of the biosensor as a consequence of the complete lack of proLC3B

96   priming. We then show that proLC3B priming can be rescued with the ectopic expression of the wild-type

97   ATG4B. Interestingly, we demonstrate that the ATG4B^{W142A} mutant, previously shown to possess a

98   significantly reduced catalytic activity [35], is capable of rescuing proLC3B priming similarly to the wild-

99   type protein. By using the LC3B biosensor and performing multiple approaches to analyze FRET/FLIM, we

100   report on the action of mechanisms of available ATG4 inhibitors. By doing so, we provide a framework of

101   how to use the LC3B biosensor and analyze the acquired data to identify new ATG4 inhibitors with better

102   specificity and efficacy.

4

Results

The LC3B biosensor dynamically reports on the activation or the inhibition of the autophagy flux, and it colocalizes with LAMP2 in an autophagy-dependent manner

To monitor the priming activity of ATG4 in real time and with spatial resolution, we developed a FRET-based biosensor that can be utilized in living cells. We chose LC3B as it is a known target of the ATG4 activity that undergoes an ATG4-mediated cleavage on Gly120, and it is among the best characterized players of the autophagy pathway [36]. The biosensor was designed to flank the N- and C-termini of proLC3B with a donor-acceptor FRET pair (Fig. 1A). The FRET pair composed of Aquamarine (donor, cyan) and tdLanYFP (acceptor, yellow) was selected on the resistance of both fluorophores to acidic pH [37–39]. In the absence of ATG4 activity, the LC3B biosensor is expected to remain unprocessed in cells, allowing Aquamarine and tdLanYFP to perform FRET (Fig. 1A). If ATG4 is active, the biosensor is expected to undergo an ATG4-dependent proteolytic cleavage at its C-terminus, thereby losing the tdLanYFP moiety and the FRET effect with it. This allows to follow the initial C-terminal priming activity of ATG4 as an early, FRET-based readout. In addition, the priming of LC3B leads to its conversion into the I form, which will still be tagged by Aquamarine (Aquamarine-LC3B-I). When the resulting Aquamarine-LC3B-I protein is integrated into the PE head groups of the phagophores, the biosensor is expected to function as a canonical fluorescent probe to quantify LC3B-positive puncta structures. Therefore, our biosensor also provides a quantitative readout on the late stages of the autophagic pathway, and it can be used to estimate the number of autophagosomes in individual cells (Fig. 1A).

We first explored whether the LC3B biosensor is capable of localizing to autophagosomes, which normally appear as puncta-shaped structures. In U2OS cells transiently transfected to express the biosensor, Aquamarine was observed to be present both in puncta-shaped structures, which are compatible with LC3B-II, and in the cytosol, which is compatible with Aqua-LC3B-I (Fig. 1B). To confirm that the puncta-shaped structures were autophagosomes, cells were treated with autophagy inducers as Torin1 or HBSS, in the

127   presence or absence of the lysosomal inhibitor Bafilomycin A_1 (BafA$_1$). Compared to control cells, a

128   significant increase in the number of Aquamarine-positive puncta was observed in cells expressing the wild-

129   type LC3B biosensor (WT biosensor) and treated with BafA$_1$ or Torin1 alone (Fig. 1B, C). A further increase

130   in the number of Aquamarine-positive puncta was observed when cells were treated simultaneously with

131   BafA$_1$ and Torin1. This indicates that the puncta-shaped structures observed under these conditions are

132   Aquamarine-LC3B-II (Aqua-LC3B-II)-positive autophagosomes, since they respond to autophagy induction

133   and to lysosomal inhibition alone or in combination. Conversely, autophagy induction by starvation did not

134   cause any increase in the number of puncta-shaped structures when compared to the control (Fig. 1B, C).

135   However, when starvation with HBSS was coupled with BafA$_1$ treatment, we observed a significant

136   accumulation of puncta-shaped structures (Fig. 1B, C). In all conditions tested, tdLanYFP appeared to be

137   diffused in the cytosol, thereby showing a dramatic difference compared to the distribution of Aquamarine

138   into puncta-shaped structures. This strongly suggests that tdLanYFP is cleaved along with the C-terminal part

139   of proLC3B, and therefore it cannot colocalize with Aquamarine on the puncta-shaped structures. To

140   corroborate this observation, we explored the distribution of an uncleavable variant of the LC3B biosensor,

141   which is mutated on Gly120 (hereby, G120A biosensor) and cannot be primed by ATG4 [36]. In cells

142   expressing the G120A biosensor, both Aquamarine and tdLanYFP were exclusively diffused in the cytosol

143   (Fig. S1), and they exhibited no puncta-shaped structures under any treatment (Fig. 1C and S1). The difference

144   in puncta numbers between the WT and the G120A biosensors supports the notion that the WT construct is

145   cleaved at the C-ter, and that it efficiently forms autophagosome-related puncta structures. In this light, we

146   verified the cleavage profiles of the WT and G120A biosensors by western blotting. While the G120A

147   biosensor had a molecular weight of ~95 kDa – corresponding to Aquamarine + proLC3B^{G120A} + tdLanYFP

148   –, the WT biosensor was cleaved in all conditions tested and appeared as two bands at ~45kDa and ~43kDa.

149   These bands were compatible with the molecular weight of Aquamarine + LC3B-I at ~45 kDa, and of

150   Aquamarine + LC3B-II at ~43 kDa (Fig. 1E). Consistent with the quantifications of puncta numbers in cells

151   expressing the WT biosensor (Fig. 1B, C), the levels of the Aqua-LC3B-II band increased upon BafA$_1$ or

Torin1 treatment, but remained unaltered upon starvation with HBSS (Fig. 1E, F). A further increase in Aqua-LC3B-II abundance was observed upon the co-treatment with BafA$_1$ and Torin1 when compared to BafA$_1$ or Torin1 alone (Fig. 1E, F). Similarly, the combination of HBSS and BafA$_1$ increased the levels of Aqua-LC3B-II when compared to HBSS alone (Fig. 1E, F). These findings suggest a rather rapid degradation of Aqua-LC3B-II via lysosomal turnover in U2OS cells upon starvation with HBSS. This also suggests that the degradation of Aqua-LC3B-II can be slowed down when starvation is coupled with a late-stage lysosomal inhibitor such as BafA$_1$. This was previously reported to occur in several other cell lines [24,40,41], and it substantiates the importance of measuring the autophagy flux in the absence or presence of lysosomal inhibitors. The differences observed in the levels of Aqua-LC3B-II were also observable at the level of the endogenous LC3B-II, confirming that the lipidation levels of the LC3B biosensor are similar to those of endogenous protein upon autophagy induction and/or lysosomal inhibition (Fig. 1E, G).

To provide conclusive evidence that Aqua-LC3B-II puncta structures are autophagosomes and are capable of colocalizing with lysosomes, we analyzed their colocalization with the lysosomal protein Lysosomal Associated Membrane Protein 2 (LAMP2). Compared to control cells, we found that the colocalization of Aqua-LC3B-II puncta structures with LAMP2-positive objects significantly increased when autophagy is induced with Torin1, but not with HBSS (Fig. 1B, D). As expected in cells expressing the WT biosensor, we observed that treatment with BafA$_1$ significantly reduced the colocalization of Aqua-LC3B-II puncta with LAMP2 compared to untreated, Torin1- or HBSS-treated cells. Conversely, the G120A biosensor did not colocalize with LAMP2 in any condition (Fig. 1D and S1). Overall, these results show that the WT biosensor colocalizes with LAMP2 in an autophagy-dependent manner.

Taken together, these results demonstrate that the LC3B biosensor is efficiently cleaved. The biosensor is capable of forming puncta structures that are consistent with the lipidated, Aqua-LC3B-II form, and they colocalize with the lysosomal protein LAMP2. The autophagy-dependent changes in the number of puncta-shaped structures or their degree of colocalization with LAMP2 indicate that the biosensor is capable of successfully reporting on autophagy induction and/or lysosomal inhibition.

The LC3B biosensor responds to the changes in proLC3B priming in an ATG4B-dependent manner

After establishing that the biosensor behaves like endogenous LC3B in cells, we sought to assess its capacity to dynamically report on LC3B processing. To this end, live cells expressing the WT or the uncleavable G120A biosensor were analyzed using FRET/FLIM. We compared the donor (Aquamarine) lifetime differences between the donor-only and the biosensor to detect FRET events, which are highlighted when the donor lifetime decreases. We then used ΔLifetime as a readout for FRET/FLIM analyses, which was determined by calculating the net difference between the lifetime of the donor-only construct (Aquamarine-proLC3B) and that of a biosensor (either Aquamarine-proLC3B- or proLC3B^{G120A}-tdLanYFP). We hypothesized that a positive ΔLifetime would be indicative of a FRET event between Aquamarine and tdLanYFP, therefore corresponding to the presence of unprimed proLC3B.

First, we measured the FRET/FLIM readout of the WT biosensor by calculating its mean ΔLifetime in the total cell area. This includes the cytosol and the puncta structures, in which the precursor, primed and lipidated forms of LC3B are expected to be present. We observed that no FRET was occurring in control cells, as illustrated by a ΔLifetime difference close to zero (Fig. 2A, B). This indicates that the LC3B biosensor is completely primed under basal conditions, leading to the loss of the tdLanYFP moiety. Conversely, the uncleavable G120A biosensor reported a significant increase of ~500 psec in ΔLifetime compared to the WT biosensor. This led us to conclude that the FRET readout of the LC3B biosensor is directly linked to its cleavage on G120. In addition, the FRET readout is specific to the biosensor constructs, as we observed no difference in ΔLifetime between the WT and G120A donor-only constructs (Fig. S2A, B).

We then reasoned that the direct correlation between FRET and priming should make the LC3B biosensor responsive to the presence or absence of ATG4. To this end, we used siRNA-mediated gene silencing to downregulate the *ATG4B* isoform, as it exhibits the highest catalytic efficiency towards LC3B compared to the other members of the ATG4 family [42]. First, we verified the efficiency of the siRNA-mediated downregulation strategy by western blotting, in cells expressing the WT or the G120A biosensor (Fig. S2C, D). When comparing the mean ΔLifetime values, no difference was observed in cells expressing

202   the G120A biosensor under any condition, as expected (Fig. 2A, B). Although no difference in mean ΔLifetime

203   was observable in control or *ATG4B*-depleted cells expressing the WT biosensor (Fig. 2A, B), we noticed the

204   presence of a significant subset of pixels exhibiting high ΔLifetime values only in *ATG4B*-depleted cells (Fig

205   2A, enlarged ΔLifetime image of the WT biosensor with *ATG4B* siRNA). Therefore, we hypothesized that

206   these pixels might correspond to unprimed proLC3B. To verify our hypothesis, we ascertained that these

207   pixels could be retrieved only upon *ATG4B* downregulation, and that they could represent unprimed pools of

208   LC3B by showing a G120A-like FRET. To this end, we performed a pixel-by-pixel FRET/FLIM analysis to

209   quantify the number of pixels showing ΔLifetime values similar or higher than the mean ΔLifetime of the

210   G120A biosensor. Indeed, *ATG4B* silencing caused a significant increase in the number of pixels with high

211   ΔLifetime values compared to the control condition (Fig. 2C). We then used the power of FRET microscopy

212   to visualize these high ΔLifetime pixels with a line analysis. This analysis allows to observe the local variations

213   in ΔLifetime occurring in the pixels crossed by a straight line. ΔLifetime values along the line went from zero

214   to the levels of the G120A biosensor only in cells silenced for *ATG4B* (Fig. 2A, D). This indicates a lack of

215   proLC3B cleavage occurring locally, and it substantiates the role of ATG4B in this process. We also noticed

216   that the increase in ΔLifetime was localized in pixels found on or near the puncta-shaped structures (Fig. 2A).

217   This reveals the spatial heterogeneity of the priming activity in these areas and uncovers a possible spatial

218   regulation of proLC3B priming, which may be taking place in discrete regions in the vicinity of

219   autophagosomes. When we performed the same analysis for donor-only constructs, we could not detect any

220   high ΔLifetime pixels, ensuring that the effect that we observe with the WT biosensor upon *ATG4B*

221   downregulation was not due to an intrinsic change in the lifetime properties of Aquamarine (Fig. S2E). To

222   make sure that the heterogeneity of ΔLifetime pixels was correctly estimated in the different conditions, we

223   analyzed the data to visualize the ΔLifetime distribution. We hypothesized that the presence of high ΔLifetime

224   pixels with G120A biosensor-like ΔLifetime values should change the overall ΔLifetime distribution. To this

225   end, we superimposed the histograms of the cells expressing the WT biosensor with or without *ATG4B*

226   depletion, and we observed a shift in the histogram mode values of *ATG4B*-depleted cells towards higher

227 ΔLifetime values (Fig. 2E). Since the mode value of a histogram corresponds to the value with the highest

228 frequency, a positive shift in the mode indicates that the ΔLifetime distribution changes due to the presence

229 of FRET events in the biosensor.

230 Considering that, in addition to its priming activity, ATG4B also acts as a deconjugating enzyme that

231 governs the ATG8ylation levels [25,43], we checked if its depletion is causing an increase in the puncta-

232 shaped structures. In cells expressing the WT biosensor or donor, we observed a robust increase in the number

233 of LC3B puncta upon *ATG4B* downregulation compared to controls (Fig. 2F, S2F). This indicates that the

234 formation of puncta-shaped structures depends on the presence of ATG4B. As expected, no puncta were

235 observed in cells expressing the G120A biosensor or donor, regardless of the presence or absence of ATG4B

236 (Fig. 2F, S2F). Similarly, when we analyzed protein levels by western blotting, we detected a significant

237 increase in the lipidated levels of the biosensor (Aqua-LC3B-II) and of the endogenous LC3B-II upon *ATG4B*

238 downregulation, compared to the controls (Fig. S2C, D).

239 Taken together, these results show that the LC3B biosensor allows to visualize changes in the ATG4B-

240 dependent priming of proLC3B. We provide evidence that the biosensor can form LC3B puncta in an ATG4B-

241 dependent manner, demonstrating that our probe recapitulates the key features of endogenous LC3B. Last, we

242 demonstrate that analyzing the FRET response of the biosensor with different modalities allows to monitor

243 the cleavage of proLC3B both at the cellular and at the subcellular level. Our findings support the pertinence

244 of this tool to spatiotemporally characterize LC3B processing in cells.

245

246 ***The total depletion of ATG4B maximizes the FRET response of the LC3B biosensor***

247 To deepen our understanding of the mode of action of the LC3B biosensor in cells, we used *ATG4* knockout

248 (KO) HeLa cells generated by Agrotis *et al.* using CRISPR/Cas9-mediated approaches [24]. First, we

249 measured the FRET response of the WT or G120A biosensor expressed in control cells. Similarly to what

250 observed in U2OS cells (Fig. 2A, B), the WT biosensor displayed a ΔLifetime close to zero, while the FLIM

251 readout of the cleavage-deficient G120A biosensor showed a ~400 psec ΔLifetime (Fig. 3A, B). When looking

252 at the distribution of the two sensors, we observed that the WT biosensor was capable of forming puncta-like

253 structures while the G120A biosensor showed a cytosolic distribution as expected (Fig. 3A). Overall, the

254 FRET behavior and the distribution of the WT and G120A LC3B biosensors were consistent with our previous

255 observations in U2OS cells.

256   We then sought to explore the FRET/FLIM readout of the LC3B biosensor in cells completely devoid

257 of the ATG4 protease. We expressed the WT biosensor in *ATG4B* single knockout (SKO) HeLa cells and in

258 comparison to control cells, the WT biosensor displayed mean ΔLifetime values of ~400 psec under these

259 conditions (Fig. 3A, B). These values were nearly identical to the mean ΔLifetime of the G120A biosensor.

260 Similarly to the distribution of the G120A biosensor, the WT biosensor in SKO cells did not exhibit noticeable

261 puncta-like structures, and it remained cytosolic. Therefore, these findings support the loss of priming of the

262 WT biosensor in an *ATG4B* SKO background. The lack of priming of the LC3B biosensor was also evident

263 in western blotting analyses (Fig. S3). The WT biosensor expressed in control cells displayed two bands

264 corresponding to the primed and the lipidated forms of the probe, both in the ~43-45 kDa range. In contrast,

265 the WT biosensor expressed in *ATG4B* SKO cells exhibited a single band at ~95 kDa. This band is similar to

266 that observed in cells expressing G120A biosensor, therefore reinforcing the conclusion that the WT biosensor

267 remains unprimed in cells lacking the ATG4B protease. We observed that the complete knockout of *ATG4B*

268 also abolishes the priming of endogenous LC3B, which exhibits a single band at 15 kDa compatible with

269 unprimed proLC3B [44] (Fig. S3). These results indicate that ATG4B is indispensable for the priming and the

270 lipidation of the LC3B biosensor.

271   We then verified whether the A and C isoforms of ATG4 family could further contribute to the priming

272 of the LC3B biosensor. The mean ΔLifetime values (Fig. 3A, B) and the western blotting profiles (Fig. S3) of

273 the WT biosensor expressed in *ATG4A/B* double knockout (DKO) or *ATG4A/B/C* triple knockout (TKO) HeLa

274 cells [24] showed no differences compared to the *ATG4B* SKO condition. This substantiates previous *in vitro*

275 reports showing that the catalytic activity of ATG4B is maximized towards LC3B [45]. To rule out every

276 possibility that the A or C isoforms could still contribute to the priming of LC3B to some extent, we increased

277   the sensitivity of our analyses by performing pixel-by-pixel FRET/FLIM calculations. We quantified the

278   number of pixels with ΔLifetime values similar or higher than the ΔLifetime of the G120A biosensor in

279   control, *ATG4B* SKO, *ATG4A/B* DKO or *ATG4A/B/C* TKO cells. With this, we aimed to explore subtle

280   changes possibly occurring between the KO cells that may remain undetected in mean ΔLifetime analyses. As

281   expected, we observed a significant increase in the number of pixels with high ΔLifetime in *ATG4B* SKO cells

282   expressing the LC3B biosensor when compared to control cells, further corroborating the results obtained with

283   mean ΔLifetime analyses (Fig. 3C). However, these analyses did not highlight any significant increase in the

284   number of pixels with high ΔLifetime upon further loss of *ATG4A* or *ATG4C* (Fig. 3C). Interestingly,

285   *ATG4A/B* DKO cells showed a slight shift towards higher ΔLifetime values in their respective histogram mode

286   value compared to the mode value of *ATG4B* SKO cells (Fig. 3D). However, only a negligible histogram

287   mode value shift was observed in *ATG4A/B/C* TKO cells compared to *ATG4A/B* DKO cells. This suggests

288   that ATG4A could still mildly contribute to the priming of the LC3B biosensor, although ATG4B is the key

289   protease in this reaction.

290   Similarly to what observed for the endogenous LC3B protein, our results demonstrate that the priming

291   of the LC3B biosensor is highly dependent on the presence of ATG4B. When *ATG4B* is absent, the LC3B

292   biosensor displays a significant FRET response, it remains unprimed and cannot be lipidated to form puncta-

293   like structures, overall resembling the behavior of the cleavage- and lipidation-deficient G120A biosensor.

294

295   ***The ectopic expression of active ATG4B rescues the priming deficiency of the LC3B biosensor in ATG4B-***

296   ***deficient cells***

297   After demonstrating that the priming of the LC3B biosensor is ATG4B-dependent, we then asked whether its

298   FRET response in ATG4B-deficient cells could be rescued by re-expressing ATG4B. To this end, we co-

299   expressed the LC3B biosensor together with an empty vector or with a vector coding for WT ATG4B. Then,

300   we evaluated the FRET/FLIM behavior of these conditions both in control and in *ATG4B* SKO cells.

301   Consistent with our previous findings (Fig. 3), the LC3B biosensor co-expressed with an empty vector in

302   *ATG4B* SKO cells showed a significant increase in its mean ΔLifetime values compared to control cells (Fig.

303   4A, B). Conversely, the expression of WT ATG4B in *ATG4B* SKO cells caused a drastic decrease in the mean

304   ΔLifetime values of the LC3B biosensor, which were close to zero. This suggests that the reintroduction of

305   WT ATG4B is sufficient to fully rescue the cleavage of the LC3 biosensor in a SKO background. Upon the

306   expression of exogenous ATG4B in control cells, we also observed that the distribution of the biosensor was

307   cytosolic and without significant puncta-like structures (Fig. 4A). On the contrary, control cells co-expressing

308   an empty vector were capable of forming puncta-like structures. This is in agreement with previous reports

309   showing that the overexpression of exogenous ATG4B blocks the lipidation of LC3B and by doing so, it leads

310   to the disappearance of LC3-positive puncta in cells [13,46,47].

311   Next, we assessed whether two mutant forms of ATG4B with different catalytic activities could rescue

312   the priming deficiency of the LC3B biosensor in *ATG4B* SKO cells. We first explored the consequences of

313   mutating the Cys74 residue of ATG4B into Ser (C74S). Cys74 belongs to a group of three aminoacids known

314   as the "catalytic triad", and its mutation into Ala or Ser was shown to cause a complete loss of the catalytic

315   activity of ATG4B [13,35]. When ATG4B^{C74S} was co-expressed with the LC3B biosensor in *ATG4B* SKO

316   cells, we measured a mean ΔLifetime comparable to *ATG4B* SKO cells transfected with an empty vector (Fig.

317   4A, B). This indicates that the catalytically-dead C74S mutant was unable to cleave and, by consequence

318   prime, the LC3B biosensor. We then tested a second mutant form of ATG4B where Trp142 was mutated into

319   Ala (W142A). Trp142 is one of the residues surrounding the catalytic triad, and its mutation into Ala was

320   reported to significantly reduce the catalytic activity of ATG4B *in vitro* [35]. Surprisingly, we observed that

321   ATG4B^{W142A} behaved similarly to WT ATG4B when expressed in SKO cells, and it resulted in a complete

322   cleavage of the LC3B biosensor in FRET/FLIM analyses (Fig. 4A, B). This supports the superior catalytic

323   efficiency of ATG4B to prime proLC3B in living cells, even in conditions where its catalytic activity is

324   severely compromised by the W142A mutation. To verify that these changes in mean ΔLifetime were specific

325   to the LC3B biosensor, we analyzed the mean ΔLifetime profiles of control or *ATG4B* SKO cells expressing

13

the donor-only Aquamarine-LC3B construct together with WT, C74S or W142A ATG4B (Fig. S4A). As expected, we did not observe any difference among all the conditions tested, further confirming that the mean ΔLifetime FRET/FLIM readout is specific towards the ATG4B-mediated cleavage of the LC3B biosensor.

We then wanted to verify if our approach based on mean ΔLifetime was sensitive enough to conclude on the capacity of the W142A mutant to fully prime LC3B. Therefore, we further evaluated the readout of the LC3B biosensor by performing pixel-by-pixel FRET/FLIM calculations, which we previously showed to be more sensitive than mean ΔLifetime analysis (Fig. 2). As expected, we observed a significant increase in the number of pixels with high ΔLifetime – indicating no LC3B priming – in *ATG4B* SKO cells co-expressing an empty vector or ATG4B^{C74S} compared to control cells (Fig. 4C). Similarly to mean ΔLifetime analyses (Fig. 4B), expressing WT ATG4B or ATG4B^{W412A} in *ATG4B* SKO cells revealed an absence of pixels with high ΔLifetime values, suggesting a complete rescue of the priming activity of the LC3B biosensor with both constructs (Fig. 4C). Accordingly, the histogram analyses of the distribution of FRET pixels in all conditions showed almost identical mode values in *ATG4B* SKO cells co-expressing WT or ATG4B^{W142A}, with their respective mode values centered around zero (Fig. 4D). On the contrary, the mode values of *ATG4B* SKO cells expressing an empty vector or ATG4B^{C74S} were drastically shifted towards 400 psec, which is again indicative of significant FRET (Fig. 4D). As expected, the analysis of the high ΔLifetime pixels in control or SKO cells expressing the donor-only Aquamarine-LC3B and each of the ATG4B constructs did not reveal any difference (Fig. S4B). Again, this substantiates the specificity of our different FRET/FLIM readouts for the LC3B biosensor only. In addition to this, the WT biosensor expressed in control cells with each of the ATG4B constructs exhibit similar histogram mode values (Fig. S4C). Nevertheless, we observed the presence of a shoulder corresponding to ΔLifetime values of ~200-300 psec in control cells co-expressing the WT biosensor with ATG4B^{C74S} (Fig. S4C), which could reflect the previously reported dominant negative effects of ATG4B^{C74S} on the soluble forms of LC3B [46].

Altogether, our results demonstrate that the proLC3B priming deficiency observed in *ATG4B* SKO cells can be fully restored when co-expressing the WT or W142A forms of ATG4B, but not with the

351 catalytically-dead C74S. Although ATG4B[W142A] was shown to display a reduced catalytic activity *in vitro*

352 [35], we demonstrate that this mutant is able to prime proLC3B in living cells similar to WT ATG4B. These

353 data were obtained with three independent methods to calculate the FRET behavior of the LC3B biosensor,

354 and they provide novel insights on the superior capacity of ATG4B to prime LC3B *in cellulo* even in

355 conditions where its catalytic activity is compromised. Importantly, they also support the notion that the

356 catalytic activity of ATG4B needs to be completely eliminated to abolish LC3B priming.

357

The LC3B biosensor reveals the mode of action of ATG4 inhibitors in cells

359 Given that the biosensor reports on the priming of LC3B by ATG4B, we sought to investigate whether it is

360 also capable to respond to pharmacological compounds that inhibit the ATG4B-LC3B axis. We first explored

361 the effect of MG132, a peptide aldehyde that inhibits both the proteasome and cysteine proteases [48,49].

362 Considering that ATG4B is a cysteine protease [14,35], we reasoned that MG132 might be able to block its

363 catalytic activity towards LC3B. Therefore, we treated HeLa cells expressing the WT or G120A biosensor

364 with DMSO or MG132, and calculated their mean ΔLifetime (Fig. S5A, B). FLIM analyses revealed a

365 significant increase in the mean ΔLifetime values of the WT biosensor in the presence of MG132. We reasoned

366 that MG132 could promote FRET within the biosensor either by inhibiting the priming activity of ATG4B, or

367 by inhibiting LC3B degradation by the proteasome. To distinguish between these two possibilities, we relied

368 on the subcellular distribution of the biosensor. In this light, the biosensor should be retrieved in the cytosol

369 in case MG132 had mainly an ATG4B-specific inhibition on proLC3B priming. Alternatively, it should rather

370 be found in puncta-like structures if this drug acted as a proteasome inhibitor. We observed a significant

371 increase in the number of Aqua-LC3B-II puncta-like structures in cells expressing the WT biosensor and

372 treated with MG132, when compared to DMSO-treated cells (Fig. S5B). Therefore, this localization of the

373 sensor in puncta-like structures suggests that MG132 is more efficient as a proteasome inhibitor, rather than a

374 specific ATG4B inhibitor. Although the number of pixels with high ΔLifetime values did not significantly

375 increase upon MG132 treatment (Fig. S5B), the histogram analysis of MG132-treated cells expressing the WT

376   biosensor revealed a mode value change when compared to DMSO-treated cells and to cells expressing the

377   G120A biosensor (Fig. S5C). Overall, this indicates that FRET events are quantitatively modest in the

378   presence of MG132, suggesting that MG132 preferentially acts as a proteasomal inhibitor rather than an

379   ATG4B-specific inhibitor. Although FRET events were limited under these conditions, we sought to explore

380   their spatial localization. Line analyses performed in cells expressing the WT biosensor and treated with

381   MG132 revealed that the ΔLifetime variations of the biosensor were of ~200 psec in the cytosol, and reaching

382   ΔLifetime values of the G120A biosensor (~400 psec) on or near the LC3B puncta (Fig. S5B, D). In contrast,

383   no fluctuations were observed in the cytosol or near puncta in control cells. These two FRET values observed

384   after treating cells with MG132 could be recapitulative of the dual action of this compound: a modest ATG4B

385   inhibitor keeping the biosensor in the cytosol, and a more potent proteasomal inhibitor on LC3B-positive

386   puncta. Of note, since Aqua-LC3B can efficiently localize on puncta-like structures (Fig. S5B) which display

387   high FRET (Fig. S5B, D), our data raise the possibility that MG132 does not alter the cleavage of tdLanYFP

388   from the biosensor. It is possible that the inhibition of proteasomal activity impairs the degradation of the

389   FRET acceptor, thereby allowing for non-specific FRET events. Therefore, these results underline the

390   importance of performing spatially-resolved, pixel-by-pixel FRET calculations to understand where and to

391   what extent the biosensor is active. They also highlight the poor efficacy of MG132 as an ATG4B-specific

392   inhibitor.

393   Afterwards, we explored the readout of the LC3B biosensor on commercially-available inhibitors with

394   better specificity than MG132 towards ATG4. Tioconazole, LV-320, FMK-9a, NSC 185058 (NSC) and *Z-L-*

395   Phe chloromethyl ketone (ZPCK) were evaluated in their capacity to inhibit the priming and/or deconjugation

396   activities of ATG4B [50–55]. These inhibitors have either been synthesized or identified in screening studies,

397   and they were previously shown to inhibit ATG4B and/or other ATG4 isoforms. They were also reported to

398   have a significant therapeutic potential in chemotherapy-resistant cancer subtypes with elevated levels of

399   autophagy [29,30].

400   We first measured the mean ΔLifetime values in HeLa cells expressing the WT or the G120A

401   biosensor, and treated or not with each of the five inhibitors. Based on our previous findings in *ATG4* KO

402   cells, we expected to observe a maximized FRET response when cells are treated with the inhibitors, along

403   with the cytosolic distribution of the WT biosensor. Within our selected set of inhibitors, two of them – NSC

404   and ZPCK – were found to significantly increase mean ΔLifetime values compared to controls (Fig. 5A vs.

405   5E, F). On the contrary, Tioconazole, LV-320 and FMK-9a did not alter the mean ΔLifetime values of the

406   biosensor (Fig. 5A-D). However, the mean ΔLifetime values of cells treated with NSC or ZPCK remained

407   lower than those of cells expressing the G120A biosensor. This suggests that the inhibitory effect of these

408   drugs towards ATG4B remains partial. We then asked whether the main function of NSC and ZPCK is to

409   inhibit the ATG4B-dependent deconjugation of LC3B or its priming. We observed a significant increase in

410   the number of Aqua-LC3B-II puncta structures upon treatment with NSC or ZPCK, further supporting the

411   idea that autophagy can still be triggered in the presence of these compounds and that the inhibition of ATG4B

412   priming activity is not complete (Fig. 5E, F). However, increased levels of Aqua-LC3B-II puncta structures

413   were observed in cells treated with Tioconazole, LV-320 or FMK-9a as well (Fig. 5B-D), and we found no

414   correlation between puncta numbers and mean ΔLifetime values with any of the inhibitors (Fig. S6). These

415   findings suggest that all the tested compounds preferentially hinder the deconjugation activity of ATG4B

416   towards LC3B, which was described to be more sensitive to ATG4B inhibition than the priming activity [56].

417   In addition to deconjugation, mean ΔLifetime differences provide the first evidence that NSC and ZPCK also

418   inhibit the priming activity of ATG4B.

419   To dissect the efficacy of the five ATG4B inhibitors with methods allowing for greater sensitivity than

420   mean ΔLifetime, we then performed high ΔLifetime-pixel counting and histogram analyses. The high

421   ΔLifetime-pixel counting analyses revealed that not only NSC and ZPCK, but also FMK-9a exhibited a

422   significantly increased number of pixels with high ΔLifetime compared to control cells (Fig. 6A-D). When

423   we analyzed the distribution of ΔLifetime pixels on histogram analyses, we observed that approximately 10-

424   20% of pixels in cells treated with NSC or ZPCK were exhibiting G120A biosensor-like ΔLifetime values.

425   These values were lowered in the presence of Tioconazole, LV-320 and FMK-9a, further corroborating the

426   superiority of NSC and ZPCK in inhibiting ATG4B (Fig. S7). In line with these findings, histogram analyses

427   revealed that NSC (113 psec) and ZPCK (150 psec) have the largest histogram mode value shift from that of

428   control cells (Fig. 6C, D). Interestingly, these analyses showed that FMK-9a, Tioconazole and LV-320 also

429   display a mode value shift from that of control cells, respectively of 74, 65 and 47 psec (Fig. 6B, S7B-C).

430   Therefore, this sensitive analysis method indicates a mild inhibition of the priming activity of ATG4B by

431   FMK-9a, Tioconazole and LV-320 as well, which was undetectable with the other analysis methods.

432   Furthermore, this approach substantiates the superior capacity of NSC and ZPCK in inhibiting ATG4B.

433   Since we observed the presence of high ΔLifetime pixels with all the inhibitors, we then sought to

434   investigate the subcellular location of these pixels using line analysis. Similarly to what observed on cells

435   silenced for *ATG4B* (Fig. 2) or treated with MG132 (Fig. S5), we noticed that high ΔLifetime pixels were

436   located either on the puncta-shaped structures, or in the surrounding area (Fig. 6 and S7). Line analyses also

437   revealed that these pixels had ΔLifetime values comparable to those of the G120A biosensor, regardless of

438   the compound used. Taken together, these findings show that ATG4B inhibition using commercially-available

439   drugs reduces the priming rates of proLC3B at discrete sites, where unprimed LC3B reservoirs can be found

440   within or in the proximity of puncta-shaped structures.

441   Overall, our data demonstrate that the LC3B FRET biosensor is a powerful tool to evaluate the mode

442   of inhibition of ATG4B-specific compounds. We also provide an innovative methodology where individual

443   sets of microscopy data can be analyzed using three independent approaches. Cumulating the information

444   obtained by the three approaches allows to spatially localize and quantify the ATG4B-dependent priming and

445   deconjugation of LC3B with unprecedented precision, and it is mandatory to characterize the mode of action

446   of present and future ATG4B-specific inhibitors.

447

Discussion

In this study, we demonstrated that the LC3B biosensor is a robust tool to monitor autophagy, as it responds to the priming and deconjugation activities of ATG4B on LC3B. We showed that these functions of ATG4B can be followed by using one single probe with a dual readout based on FRET, and on the accumulation of the probe on autophagosomes.

Among the several approaches available to monitor autophagy, the most widely used assays rely on the use of single fluorescent protein (FP)-tagged LC3B probes to quantify the number of autophagosomes [57]. The LC3B biosensor retains this property, since it functions as a standard single FP-tagged probe after LC3B is primed. We also show that the biosensor reports on autophagy induction and/or inhibition while colocalizing with the lysosomal marker protein LAMP2 in an autophagy-dependent manner, similarly to other LC3B-based fluorescent constructs. Since the LC3B biosensor is constituted of a pair of FPs resistant to acidic pH, its readout can be followed throughout the entire autophagy pathway. Importantly, the LC3B biosensor has the capacity to respond to proLC3B priming in living cells, thanks to these FPs behaving as a donor-acceptor FRET pair. The proLC3B priming by ATG4s is among the earliest events occurring when autophagy is triggered [13,36]. A FRET-based strategy relying on a CFP/YFP donor-acceptor pair has already been used to measure the enzymatic activity of ATG4A and ATG4B towards the ATG8 family in a purely *in vitro* system [58]. However, this strategy has never been implemented in living cells, most likely due to the lack of yellow FPs retaining their acceptor properties in conditions of acidic pH. The recent development of tdLanYFP [39] allowed us to create an LC3B biosensor suitable for living cells. By following the FRET behavior of the biosensor, we showed that the probe responds to the ATG4B-dependent changes in proLC3B priming. It was previously reported that proLC3B is primed nearly instantaneously after translation, due to the constitutive proteolytic activity of ATG4B [36,59]. In line with this, we found that the LC3B biosensor was almost completely primed under basal conditions, without any detectable accumulation of proLC3B in cells. In contrast, we showed that the proLC3B priming activity is altered in cells silenced for *ATG4B*, and that the

472 unprimed biosensor is located on or in close vicinity of puncta-shaped structures. Since the priming activity

473 of ATG4B is more efficient than its deconjugation activity, alterations in ATG4B levels were shown to mostly

474 affect deconjugation rather than priming [56]. Our findings using the LC3B biosensor were complementary

475 to this notion, as we were able to observe a stark increase in the number of Aqua-LC3B-II puncta structures

476 when *ATG4B* was silenced. By using a combination of broad and sensitive approaches to quantify FRET, we

477 provided the first proof of concept that proLC3B priming events occur at discrete sites in cells. It is likely that

478 these sites are already present to a lower extend under basal conditions, and they are highlighted only when

479 ATG4B priming activity is altered. With microscopy approaches with higher resolution, it might be possible

480 to reveal the existence of these reservoirs under basal conditions as well. In this light, the LC3B FRET

481 biosensor has the unique capacity to identify these priming reservoirs in living cells and with subcellular

482 resolution, underlining the superior sensitivity of the LC3B biosensor to explore the functional relevance of

483 these structures and the proteins regulating their formation.

484 Furthermore, we confirmed that the isoform ATG4B is the major cysteine protease priming the LC3B

485 biosensor, and that its knockout results in a complete lack of priming. Additionally, we provided evidence that

486 ATG4A could mildly contribute to the priming of the LC3B biosensor in the absence of ATG4B, corroborating

487 previous findings concerning a functional redundancy among these isoforms [24,60]. Interestingly, our

488 biosensor provided novel information on the relevance of specific ATG4B residues for its priming activity. In

489 this light, we observed an unexpected ability of mutant ATG4B^{W142A} to fully prime proLC3B. Trp142 localizes

490 near the catalytic Cys74 residue, and it was suggested to be responsible for LC3 tail recognition [35]. In *in*

491 *vitro* cleavage assays, ATG4B with mutated Trp142 displayed a significantly reduced ability to cleave C-

492 terminally tagged LC3 [35]. Based on these findings, we were expecting to observe a reduced LC3B priming

493 with ATG4B^{W142A}, and no priming was expected with the catalytically-dead mutant ATG4B^{C74S}. While

494 ATG4B^{C74S} was incapable of priming proLC3B, we observed a full priming of the LC3B biosensor in the

495 presence of the ATG4B^{W142A} construct. Not only these results corroborate the high efficiency of ATG4B to

cleave proLC3B even in conditions where its catalytic activity is severely reduced, but they also highlight a drastic difference between *in vitro* findings and data obtained in more complex paradigms.

Given the rising interest in developing inhibitors that block the early stages of autophagy by targeting ATG4B, we challenged the LC3B biosensor with a selection of available inhibitors. Again, our biosensor demonstrated to be a useful tool to investigate the mode of action and the efficacy of these compounds at the concentrations and timepoints chosen for the analyses. First, we observed increased amounts of Aqua-LC3B-II puncta after the incubation with all the inhibitors, indicating a reduction in the deconjugation activity of ATG4B. These results were not surprising, as the deconjugation activity of ATG4B was reported to be less efficient than the priming, and therefore more prone to get affected upon inhibition [56]. Furthermore, our data also show that none of the inhibitors was able to completely abolish the priming activity of ATG4B towards LC3B. Indeed, we did not observe a cytosolic distribution of the LC3B biosensor, nor ΔLifetime values similar to those measured with the priming-defective G120A biosensor. Despite an incomplete inhibition on priming, we found that the cells treated with NSC or ZPCK exhibited a significant reduction in LC3B priming compared to control cells. Cells treated with MG132 – a proteasome inhibitor with a capacity to inhibit cysteine proteases [48,49] – exhibited a significant increase in the mean ΔLifetime values, along with a positive shift in the histogram mode value. In contrast, they did not display significant amounts of pixels with high ΔLifetime. It is possible that the incubation with MG132 does not prevent the complete degradation of tdLanYFP once this moiety has been cleaved from the biosensor. In this case, the presence of tdLanYFP in the close vicinity of Aqua-LC3B-II puncta would lead to unspecific FRET events, potentially unrelated to the proLC3B priming readout of the biosensor. This is the reason why a multi-parameter FRET quantification – mean ΔLifetime, number of pixels with high ΔLifetime, histogram distribution of the ΔLifetime values – is mandatory to characterize the specificity of ATG4B inhibitors. In this light, we propose that an efficient ATG4B inhibitor should display a significant difference from controls in the three methods of analysis. A compound that did not meet all the criteria but still displayed a significant increase in the number of high-ΔLifetime pixels with a positive histogram mode value shift was FMK-9a. Although FMK-based

521   compounds were shown to be very potent ATG4B inhibitors [30,52,61], a recent study showed that FMK-9a

522   induces autophagy independently of its inhibition on ATG4B activity [53]. Therefore, our findings support

523   these results since FMK-9a did not meet all the criteria to be considered as an efficient ATG4B inhibitor.

524   Finally, our results on Tioconazole and LV-320 indicate that these two compounds inhibit the priming of

525   proLC3B to a lesser extent than the other compounds. Since they only displayed a positive shift in the

526   histogram mode values and did not meet any other criteria, we propose that they should be considered as mild

527   ATG4B inhibitors. Overall, our results underline the lack of inhibitors that can fully inhibit the priming activity

528   of ATG4B. Future screenings using the LC3B biosensor will be useful to identify new inhibitory compounds,

529   as one would expect to observe a FRET behavior similar to that of the G120A biosensor or *ATG4* KO cells in

530   case of a full inhibition of proLC3B priming.

531   Since it is possible to calculate the number of pixels with high ΔLifetime, additional information can

532   be provided by localizing these pixels at the subcellular level. We observed a consistent presence of pixels

533   with high ΔLifetime around or on puncta-shaped structures, either upon ATG4B inhibition or *ATG4B*

534   silencing. In this light, we suggest that the local scarcity or the inhibition of ATG4B may cause alterations in

535   the proLC3B priming rates in discrete areas of the autophagosomes, which could be considered as priming

536   "hotspots". As previously mentioned, these reservoirs or "hotspots" with reduced proLC3B priming rates may

537   be sites where proLC3B is temporarily stored while trying to re-establish the full priming capacity of ATG4B.

538   Overall, we present the LC3B biosensor as a second-generation FRET biosensor that can report on the

539   regulation of the soluble and the lipidated forms of LC3B by ATG4B. First, this tool can be used to infer on

540   the structural properties of ATG4B and on its enzymatic activity. Thanks to its dual FRET/localization

541   readout, it can also be used to follow LC3B priming and turnover with superior spatiotemporal resolution.

542   Finally, the LC3B biosensor has the potential to be used in high-content screenings to identify more potent

543   ATG4B inhibitors and reveal their mode of action in living cells, which is a unique feature of the biosensor

544   compared to *in vitro* screening methodologies. Thus, the LC3B biosensor paves the way to ATG4B-targeted

545   therapies in complex diseases.

Materials and Methods

Expression vectors and molecular cloning

All the plasmids used in this study are listed in Supplementary Table 1. The cloning reactions were performed using the Gibson Assembly Master Mix (New England Biolabs). Site-directed mutagenesis was performed with the Quik-Change kit (Agilent). All the constructs from cloning and mutagenesis reactions were verified using a 3130 XL sequencer (Applied Biosystems) and a BigDye Terminator V3.1 sequencing kit (Applied Biosystems).

Cell culture and transfections

U2OS cells (HTB-96) were purchased from American Type Culture Collection. Control and *ATG4* KO HeLa cells were kind gifts of Dr. Robin Ketteler (UCL, LMCB, United Kingdom). Cells were cultured in DMEM (Thermo Fisher Scientific) supplemented with 10% FBS (Eurobio Scientific) and penicillin-streptomycin (100 U/mL, Thermo Fisher Scientific) and maintained at 37°C with 5% CO_2. All cell lines were routinely checked for the absence of mycoplasma. Before imaging, normal growth media was replaced with phenol red-free Leibovitz's L-15 medium (Thermo Fisher Scientific) supplemented with 20% FBS and penicillin-streptomycin (100 U/mL). Cells were seeded at 70% confluence in Nunc Lab-Tek II Chamber slides (Thermo Fisher Scientific) or Cellview cell culture slides (Greiner bio-one, 543979) for live cell imaging, 24-well plates for immunocytochemistry, or 6-well plates for total cell lysates. Plasmid DNA transfection, or plasmid DNA and siRNA co-transfection experiments were performed using Lipofectamine 2000 (Invitrogen) according to the manufacturer's instructions. Cells were analyzed 48h after transfection. AllStars negative control siRNA (SI03650318) and the *ATG4B*-specific siRNA (SI03156314) were purchased from QIAGEN.

Chemical compounds

The chemical compounds used in this study were as follows: Bafilomycin A1 (Sigma-Aldrich, B1793), FMK 9a (MedChemExpress, HY-100522), LV-320 (MedChemExpress, HY-112711), MG-132 (Selleckchem, S2619), NSC 185058 (Selleckchem, S6716), Tioconazole (Sigma-Aldrich, 03907), Torin1 (Sigma-Aldrich, 475991), *Z-L*-Phe chloromethyl ketone (Sigma-Aldrich, 860794). All chemical compounds were dissolved in dimethyl sulfoxide (Sigma-Aldrich, D2438) and stored at -80°C. For starvation assay, a home-made Hank's Balanced Salt Solution (HBSS) containing 8 mg/ml NaCl, 0.4 mg/ml KCl, 0.06 mg/ml KH_2PO_4, 0.048 mg/ml Na_2HPO_4 anhydrous, 1 mg/ml glucose, 0.348 mg/ml $NaHCO_3$ and penicillin-streptomycin (100 U/mL) was used. Concentrations and durations of each treatment are indicated in the figure legends.

Western blotting

To collect total cell lysates, cells were rinsed with ice-cold Phosphate Buffer Saline (PBS) (Euromedex, ET330-A) and lysed on ice in a buffer containing 50 mM Tris-HCL (pH 7.4), 150 mM NaCl, 1% Triton X-100 (Euromedex, 2000-A), 1.5 mM $MgCl_2$, supplemented with 0.2 mM Na_3VO_4, 0.5 mM DTT (Thermo Fisher Scientific, R0861), 4 mg/ml NaF, 5.4 mg/ml β-glycerolphosphate and a protease inhibitor cocktail (Roche, 11873580001) immediately prior to lysis. Lysates were centrifuged at 13000 *g* for 20 minutes at 4°C. Protein levels were quantified by using the Bradford protein assay dye reagent (BioRad, 5000006). Lysates were then heated in Laemmli sample buffer at 95°C for 5 minutes, resolved in home-made Acrylamide/Bis 37.5:1 SDS-PAGE mini gels and transferred onto nitrocellulose membrane (Amersham™ Protran®, 10600004). Membranes were blocked in a solution containing 5% skimmed milk in TBS-T (TBS [Euromedex, ET220] containing 0.1% Tween [Euromedex, 2001-B]) and incubated overnight at 4°C with primary antibodies diluted in the blocking solution. The next day, membrane was washed in TBS-T, incubated with the secondary antibody diluted in the blocking solution for 1h at room temperature, and washed again in TBS-T prior to detection. The primary antibodies and dilutions were as follows: rabbit anti-Actin (Sigma-Aldrich, A5060; 1:1000), ATG4B (Cell Signaling, 5299; 1:1000), LC3B (Cell Signaling, 3868; 1:1000). The secondary antibody used was a horseradish-peroxidase-conjugated goat anti-rabbit antibody (Jackson ImmunoResearch;

594   1:6000-1:10000). After incubating the membrane in an ECL western blotting substrate (Thermo Fisher

595   Scientific, 32209), chemiluminescence signals were captured on a film (Thermo Fisher Scientific, 34091) and

596   developed with a CURIX 60 developer (Agfa Healthcare). The density of the bands was quantified by using

597   the *Gel Analyzer* function in Fiji (NIH) software. The relative abundance of each band was calculated by

598   normalizing the density of the band to that of the respective loading control.

599

600   *Immunocytochemistry, confocal and FLIM microscopy*

601   For immunocytochemistry, cells were seeded on 15 mm round coverslips placed onto 24-well plates. Cells

602   were washed with 1X PBS and fixed in 1X PBS containing a mixture of 4% paraformaldehyde (Electron

603   Microscopy Sciences, 15710) and 0.2% Glutaraldehyde (Euromedex, EM-16221) at room temperature for 20

604   minutes. After washing in 1X PBS, cells were permeabilized with 0.2% Triton in PBS for 10 minutes, washed

605   again in 1X PBS and blocked for 1h in 5% BSA (Euromedex, 04-100-812-C) in 1X PBS at room temperature.

606   Cells were incubated overnight at 4°C with primary antibodies diluted in the blocking buffer, and then washed

607   with 1X PBS. Cells were then incubated with the secondary antibody diluted in the blocking buffer for 45

608   minutes at room temperature. Primary monoclonal anti-LAMP2 (Abcam, ab25631; 1:200) was used as a

609   primary antibody and a goat anti-mouse IgG (H+L) cross-adsorbed antibody Alexa Fluor™ 647 (Thermo

610   Fisher Scientific, A-21235; 1:500) was used as a secondary antibody. After washing in 1X PBS, coverslips

611   were mounted in ProLong Gold Antifade reagent (Invitrogen, P36930). Cells were imaged with a Leica SP8

612   inverted confocal microscope equipped with a 63x oil immersion objective (NA 1.4). Aquamarine

613   fluorescence was acquired with a 440 nm excitation laser, and an emission wavelength of 467-499 nm. The

614   fluorescence of tdLanYFP and of LAMP2/Alexa 647 were captured by using a 514 nm and a 633 nm argon

615   laser, respectively. The emission wavelengths were 525-565 nm for tdLanYFP, and 650-720 nm for

616   LAMP2/Alexa 647. For FLIM analyses, images were acquired with a time-gated custom-made setup based

617   on a spinning disk microscope as described in [62]. Aquamarine was used as a FRET donor in all experiments,

618   and excited at 440 ± 10 nm with a supercontinuum picosecond pulsed laser source. Emission was selected

619 using a band pass filter of 483/35 nm. The FLIM setup was controlled by the Inscoper Suite solution (Inscoper,

620 France), and Aquamarine lifetime was measured in real-time during acquisition with the Inscoper software.

621

622 *Image analysis*

623 All the image analysis were performed in Fiji software. 3D puncta counting and fluorescence colocalization

624 analyses illustrated in Fig. 1B-D and Fig. S1 were performed by using the macro developed by Cordelières

625 and Zhang [63] in batch processing mode, and available in a GitHub repository at

626 https://github.com/NEUBIAS/neubias-springer-book-2020. The minimum size of the objects for Aquamarine-

627 LC3B and LAMP2/Alexa 647 was set to 10 voxels. The threshold to separate the objects from the background

628 was set manually for both channels. The total number of objects in Aquamarine-LC3B channel was used to

629 determine the number of Aqua-LC3B-II puncta-shaped structures. The objects in the Aquamarine-LC3B

630 channel superposing with the LAMP2/Alexa 647 objects were used for colocalization analyses, and only the

631 Aquamarine-LC3B objects superposing with the LAMP2/Alexa 647 objects with a ratio of 0.5 or more were

632 quantified for analyses. The colocalizing objects were then normalized to the total number of Aquamarine-

633 LC3B objects. For FLIM analysis, mean ΔLifetime values were calculated as previously described [38]. In all

634 experiments, Aquamarine lifetime was calculated by the Inscoper software only when the pixel-by-pixel

635 fluorescence intensity in the first gate was above 1000 grey levels. The number of Aqua-LC3B-II puncta

636 structures in the accompanying fluorescence images (Fig. 2A, S2A, 5A-F, S5A-B) were quantified using the

637 *Find Maxima* function in the Fiji imaging software, and by setting the prominence value as 1500. To analyze

638 the high-ΔLifetime pixels, the *Histogram* tool in Fiji was used to measure the number of pixels with a lifetime

639 between 2000 and 4000 psec. Each histogram was then converted to a ΔLifetime format by using the mean

640 lifetime value of the donor-only construct as a normalizer. To determine the number of pixels with high

641 ΔLifetime, the mean ΔLifetime value of the G120A biosensor or the mean ΔLifetime value of the WT

642 biosensor expressed in *ATG4B* SKO cells were used as a threshold. The number of pixels showing G120A

643 biosensor-like ΔLifetime or higher were then quantified and normalized to the total number of pixels, and this

644   to determine the high-ΔLifetime pixel ratio per cell. For line analysis, a 17.8 µm linear region of interest (ROI)

645   that contains both the high- and low-ΔLifetime pixels was manually drawn near or on the puncta-like

646   structures. The *Plot profile* function in Fiji was then used to obtain ΔLifetime values on the drawn line, which

647   were then plotted. For histogram analyses, the average number of pixels per ΔLifetime was quantified for each

648   condition.

649

650   *Statistical analysis*

651   All statistical tests were performed by using GraphPad Prism 9. Two-way ANOVA with Tukey method was

652   applied to make multiple comparisons in the following figures: 1C-D; 2B-C, F; 3B-C; 4B-C; 5B-F; 6B-D;

653   S2B, F; S4A-B; S5B; S7B-C. Two-way ANOVA with two-stage step-up method of Benjamini, Krieger and

654   Yekutieli was applied to make multiple comparisons in the following figures: 1F-G and S2D. Correlation

655   analysis between the ΔLifetime values and the puncta numbers were performed to compute R^2 and P values

656   in Fig. S6.

657

658   *Figure preparation*

659   The cartoon in Figure 1A was prepared by using the illustrations available at https://smart.servier.com/ [64].

660   Graphs and figures were assembled in GraphPad Prism 9 and Inkscape, respectively.

661

662   *Data and material availability*

663   Plasmids and macro used in this study and the source data that support the findings are available from the

664   corresponding authors (G.B. [giulia.bertolin@univ-rennes1.fr] and M.T. [marc.tramier@univ-rennes1.fr]) on

665   request.

666

Acknowledgments

Author Contributions

E.B.G. designed, performed and analyzed the experiments and wrote the manuscript; A.C. performed the experiments and revised the manuscript, M.T. co-supervised the work, revised the manuscript and provided funding; G.B. co-supervised the work, designed the experiments, edited and revised the manuscript, and provided funding.

Conflict of interest

The authors declare no conflict of interest.

References

1. Ohsumi, Y. Historical Landmarks of Autophagy Research. *Cell Research* **2014**, *24*, 9–23, doi:10.1038/cr.2013.169.

2. Klionsky, D.J.; Emr, S.D. Autophagy as a Regulated Pathway of Cellular Degradation. *Science* **2000**, *290*, 1717–1721, doi:10.1126/science.290.5497.1717.

3. Deretic, V.; Levine, B. Autophagy, Immunity, and Microbial Adaptations. *Cell Host & Microbe* **2009**, *5*, 527–549, doi:10.1016/j.chom.2009.05.016.

4. Rodriguez-Rocha, H.; Garcia-Garcia, A.; Panayiotidis, M.I.; Franco, R. DNA Damage and Autophagy. *Mutation Research/Fundamental and Molecular Mechanisms of Mutagenesis* **2011**, *711*, 158–166, doi:10.1016/j.mrfmmm.2011.03.007.

5. Axe, E.L.; Walker, S.A.; Manifava, M.; Chandra, P.; Roderick, H.L.; Habermann, A.; Griffiths, G.; Ktistakis, N.T. Autophagosome Formation from Membrane Compartments Enriched in Phosphatidylinositol 3-Phosphate and Dynamically Connected to the Endoplasmic Reticulum. *J Cell Biol* **2008**, *182*, 685–701, doi:10.1083/jcb.200803137.

6. Mizushima, N.; Yoshimori, T.; Ohsumi, Y. The Role of Atg Proteins in Autophagosome Formation. *Annu Rev Cell Dev Biol* **2011**, *27*, 107–132, doi:10.1146/annurev-cellbio-092910-154005.

7. Ichimura, Y.; Kirisako, T.; Takao, T.; Satomi, Y.; Shimonishi, Y.; Ishihara, N.; Mizushima, N.; Tanida, I.; Kominami, E.; Ohsumi, M.; et al. A Ubiquitin-like System Mediates Protein Lipidation. *Nature* **2000**, *408*, 488–492, doi:10.1038/35044114.

8. Weidberg, H.; Shvets, E.; Shpilka, T.; Shimron, F.; Shinder, V.; Elazar, Z. LC3 and GATE-16/GABARAP Subfamilies Are Both Essential yet Act Differently in Autophagosome Biogenesis. *The EMBO Journal* **2010**, *29*, 1792–1802, doi:10.1038/emboj.2010.74.

9. Noda, N.N.; Ohsumi, Y.; Inagaki, F. Atg8-Family Interacting Motif Crucial for Selective Autophagy. *FEBS Letters* **2010**, *584*, 1379–1385, doi:10.1016/j.febslet.2010.01.018.

714 10. Shpilka, T.; Weidberg, H.; Pietrokovski, S.; Elazar, Z. Atg8: An Autophagy-Related Ubiquitin-like
715   Protein Family. *Genome Biology* **2011**, *12*, 226, doi:10.1186/gb-2011-12-7-226.

716 11. Jatana, N.; Ascher, D.B.; Pires, D.E.V.; Gokhale, R.S.; Thukral, L. Human LC3 and GABARAP
717   Subfamily Members Achieve Functional Specificity via Specific Structural Modulations. *Autophagy*
718   **2020**, *16*, 239–255, doi:10.1080/15548627.2019.1606636.

719 12. Kirisako, T.; Ichimura, Y.; Okada, H.; Kabeya, Y.; Mizushima, N.; Yoshimori, T.; Ohsumi, M.; Takao,
720   T.; Noda, T.; Ohsumi, Y. The Reversible Modification Regulates the Membrane-Binding State of
721   Apg8/Aut7 Essential for Autophagy and the Cytoplasm to Vacuole Targeting Pathway. *J Cell Biol* **2000**,
722   *151*, 263–276, doi:10.1083/jcb.151.2.263.

723 13. Tanida, I.; Sou, Y.; Ezaki, J.; Minematsu-Ikeguchi, N.; Ueno, T.; Kominami, E.
724   HsAtg4B/HsApg4B/Autophagin-1 Cleaves the Carboxyl Termini of Three Human Atg8 Homologues
725   and Delipidates Microtubule-Associated Protein Light Chain 3- and GABAA Receptor-Associated
726   Protein-Phospholipid Conjugates. *J Biol Chem* **2004**, *279*, 36268–36276, doi:10.1074/jbc.M401461200.

727 14. Kabeya, Y.; Mizushima, N.; Yamamoto, A.; Oshitani-Okamoto, S.; Ohsumi, Y.; Yoshimori, T. LC3,
728   GABARAP and GATE16 Localize to Autophagosomal Membrane Depending on Form-II Formation.
729   *Journal of Cell Science* **2004**, *117*, 2805–2812, doi:10.1242/jcs.01131.

730 15. Hanada, T.; Noda, N.N.; Satomi, Y.; Ichimura, Y.; Fujioka, Y.; Takao, T.; Inagaki, F.; Ohsumi, Y. The
731   Atg12-Atg5 Conjugate Has a Novel E3-like Activity for Protein Lipidation in Autophagy. *J Biol Chem*
732   **2007**, *282*, 37298–37302, doi:10.1074/jbc.C700195200.

733 16. Martens, S.; Fracchiolla, D. Activation and Targeting of ATG8 Protein Lipidation. *Cell Discov* **2020**, *6*,
734   1–11, doi:10.1038/s41421-020-0155-1.

735 17. Nakatogawa, H.; Ichimura, Y.; Ohsumi, Y. Atg8, a Ubiquitin-like Protein Required for Autophagosome
736   Formation, Mediates Membrane Tethering and Hemifusion. *Cell* **2007**, *130*, 165–178,
737   doi:10.1016/j.cell.2007.05.021.

18. Xie, Z.; Nair, U.; Klionsky, D.J. Atg8 Controls Phagophore Expansion during Autophagosome Formation. *Mol Biol Cell* **2008**, *19*, 3290–3298, doi:10.1091/mbc.E07-12-1292.

19. Pankiv, S.; Clausen, T.H.; Lamark, T.; Brech, A.; Bruun, J.-A.; Outzen, H.; Øvervatn, A.; Bjørkøy, G.; Johansen, T. P62/SQSTM1 Binds Directly to Atg8/LC3 to Facilitate Degradation of Ubiquitinated Protein Aggregates by Autophagy. *J Biol Chem* **2007**, *282*, 24131–24145, doi:10.1074/jbc.M702824200.

20. Mizushima, N. The ATG Conjugation Systems in Autophagy. *Current Opinion in Cell Biology* **2020**, *63*, 1–10, doi:10.1016/j.ceb.2019.12.001.

21. Nair, U.; Yen, W.-L.; Mari, M.; Cao, Y.; Xie, Z.; Baba, M.; Reggiori, F.; Klionsky, D.J. A Role for Atg8–PE Deconjugation in Autophagosome Biogenesis. *Autophagy* **2012**, *8*, 780–793, doi:10.4161/auto.19385.

22. Nakatogawa, H.; Ishii, J.; Asai, E.; Ohsumi, Y. Atg4 Recycles Inappropriately Lipidated Atg8 to Promote Autophagosome Biogenesis. *Autophagy* **2012**, *8*, 177–186, doi:10.4161/auto.8.2.18373.

23. Yu, Z.-Q.; Ni, T.; Hong, B.; Wang, H.-Y.; Jiang, F.-J.; Zou, S.; Chen, Y.; Zheng, X.-L.; Klionsky, D.J.; Liang, Y.; et al. Dual Roles of Atg8−PE Deconjugation by Atg4 in Autophagy. *Autophagy* **2012**, *8*, 883–892, doi:10.4161/auto.19652.

24. Agrotis, A.; Pengo, N.; Burden, J.J.; Ketteler, R. Redundancy of Human ATG4 Protease Isoforms in Autophagy and LC3/GABARAP Processing Revealed in Cells. *Autophagy* **2019**, *15*, 976–997, doi:10.1080/15548627.2019.1569925.

25. Nguyen, T.N.; Padman, B.S.; Zellner, S.; Khuu, G.; Uoselis, L.; Lam, W.K.; Skulsuppaisarn, M.; Lindblom, R.S.J.; Watts, E.M.; Behrends, C.; et al. ATG4 Family Proteins Drive Phagophore Growth Independently of the LC3/GABARAP Lipidation System. *Mol Cell* **2021**, *81*, 2013-2030.e9, doi:10.1016/j.molcel.2021.03.001.

26. Betin, V.M.S.; Singleton, B.K.; Parsons, S.F.; Anstee, D.J.; Lane, J.D. Autophagy Facilitates Organelle Clearance during Differentiation of Human Erythroblasts: Evidence for a Role for ATG4 Paralogs during Autophagosome Maturation. *Autophagy* **2013**, *9*, 881–893, doi:10.4161/auto.24172.

763   27. Levine, B.; Kroemer, G. Biological Functions of Autophagy Genes: A Disease Perspective. *Cell* **2019**,

764   *176*, 11–42, doi:10.1016/j.cell.2018.09.048.

765   28. Galluzzi, L.; Bravo-San Pedro, J.M.; Levine, B.; Green, D.R.; Kroemer, G. Pharmacological Modulation

766   of Autophagy: Therapeutic Potential and Persisting Obstacles. *Nature Reviews Drug Discovery* **2017**,

767   *16*, 487–511, doi:10.1038/nrd.2017.22.

768   29. Ariosa, A.R.; Lahiri, V.; Lei, Y.; Yang, Y.; Yin, Z.; Zhang, Z.; Klionsky, D.J. A Perspective on the Role

769   of Autophagy in Cancer. *Biochimica et Biophysica Acta (BBA) - Molecular Basis of Disease* **2021**, *1867*,

770   166262, doi:10.1016/j.bbadis.2021.166262.

771   30. Agrotis, A.; Ketteler, R. On ATG4B as Drug Target for Treatment of Solid Tumours-The Knowns and

772   the Unknowns. *Cells* **2019**, *9*, E53, doi:10.3390/cells9010053.

773   31. *Principles of Fluorescence Spectroscopy*;

774   32. Truong, K.; Ikura, M. The Use of FRET Imaging Microscopy to Detect Protein–Protein Interactions and

775   Protein Conformational Changes in Vivo. *Current Opinion in Structural Biology* **2001**, *11*, 573–578,

776   doi:10.1016/S0959-440X(00)00249-9.

777   33. Sizaire, F.; Tramier, M. FRET-Based Biosensors: Genetically Encoded Tools to Track Kinase Activity

778   in Living Cells. *Protein Phosphorylation* **2017**, doi:10.5772/intechopen.71005.

779   34. Padilla-Parra, S.; Tramier, M. FRET Microscopy in the Living Cell: Different Approaches, Strengths

780   and Weaknesses. *Truong & Ikura* **2012**, *34*, 369–376, doi:10.1002/bies.201100086.

781   35. Sugawara, K.; Suzuki, N.N.; Fujioka, Y.; Mizushima, N.; Ohsumi, Y.; Inagaki, F. Structural Basis for

782   the Specificity and Catalysis of Human Atg4B Responsible for Mammalian Autophagy. *J Biol Chem*

783   **2005**, *280*, 40058–40065, doi:10.1074/jbc.M509158200.

784   36. Kabeya, Y.; Mizushima, N.; Ueno, T.; Yamamoto, A.; Kirisako, T.; Noda, T.; Kominami, E.; Ohsumi,

785   Y.; Yoshimori, T. LC3, a Mammalian Homologue of Yeast Apg8p, Is Localized in Autophagosome

786   Membranes after Processing. *EMBO J* **2000**, *19*, 5720–5728, doi:10.1093/emboj/19.21.5720.

787 37. Erard, M.; Fredj, A.; Pasquier, H.; Beltolngar, D.-B.; Bousmah, Y.; Derrien, V.; Vincent, P.; Merola, F.

788   Minimum Set of Mutations Needed to Optimize Cyan Fluorescent Proteins for Live Cell Imaging. *Mol.*

789   *BioSyst.* **2013**, *9*, 258–267, doi:10.1039/C2MB25303H.

790 38. Bertolin, G.; Sizaire, F.; Déméautis, C.; Chapuis, C.; Mérola, F.; Erard, M.; Tramier, M. Optimized

791   FRET Pairs and Quantification Approaches To Detect the Activation of Aurora Kinase A at Mitosis.

792   *ACS Sens* **2019**, *4*, 2018–2027, doi:10.1021/acssensors.9b00486.

793 39. Bousmah, Y.; Valenta, H.; Bertolin, G.; Singh, U.; Nicolas, V.; Pasquier, H.; Tramier, M.; Merola, F.;

794   Erard, M. TdLanYFP, a Yellow, Bright, Photostable, and PH-Insensitive Fluorescent Protein for Live-

795   Cell Imaging and Förster Resonance Energy Transfer-Based Sensing Strategies. *ACS Sens* **2021**, *6*,

796   3940–3947, doi:10.1021/acssensors.1c00874.

797 40. Tanida, I.; Minematsu-Ikeguchi, N.; Ueno, T.; Kominami, E. Lysosomal Turnover, but Not a Cellular

798   Level, of Endogenous LC3 Is a Marker for Autophagy. *Autophagy* **2005**, *1*, 84–91,

799   doi:10.4161/auto.1.2.1697.

800 41. Nash, Y.; Schmukler, E.; Trudler, D.; Pinkas-Kramarski, R.; Frenkel, D. DJ-1 Deficiency Impairs

801   Autophagy and Reduces Alpha-Synuclein Phagocytosis by Microglia. *J Neurochem* **2017**, *143*, 584–594,

802   doi:10.1111/jnc.14222.

803 42. Li, M.; Hou, Y.; Wang, J.; Chen, X.; Shao, Z.-M.; Yin, X.-M. Kinetics Comparisons of Mammalian Atg4

804   Homologues Indicate Selective Preferences toward Diverse Atg8 Substrates. *J Biol Chem* **2011**, *286*,

805   7327–7338, doi:10.1074/jbc.M110.199059.

806 43. Agrotis, A.; von Chamier, L.; Oliver, H.; Kiso, K.; Singh, T.; Ketteler, R. Human ATG4 Autophagy

807   Proteases Counteract Attachment of Ubiquitin-like LC3/GABARAP Proteins to Other Cellular Proteins.

808   *Journal of Biological Chemistry* **2019**, *294*, 12610–12621, doi:10.1074/jbc.AC119.009977.

809 44. Wang, W.; Chen, Z.; Billiar, T.R.; Stang, M.T.; Gao, W. The Carboxyl-Terminal Amino Acids Render

810   Pro-Human LC3B Migration Similar to Lipidated LC3B in SDS-PAGE. *PLOS ONE* **2013**, *8*, e74222,

811   doi:10.1371/journal.pone.0074222.

45. Li, M. Kinetics Comparisons of Mammalian Atg4 Homologues Indicate Selective Preferences toward Diverse Atg8 Substrates*. **2011**, *286*, 12.

46. Fujita, N.; Hayashi-Nishino, M.; Fukumoto, H.; Omori, H.; Yamamoto, A.; Noda, T.; Yoshimori, T. An Atg4B Mutant Hampers the Lipidation of LC3 Paralogues and Causes Defects in Autophagosome Closure. *Mol Biol Cell* **2008**, *19*, 4651–4659, doi:10.1091/mbc.e08-03-0312.

47. Skytte Rasmussen, M.; Mouilleron, S.; Kumar Shrestha, B.; Wirth, M.; Lee, R.; Bowitz Larsen, K.; Abudu Princely, Y.; O'Reilly, N.; Sjøttem, E.; Tooze, S.A.; et al. ATG4B Contains a C-Terminal LIR Motif Important for Binding and Efficient Cleavage of Mammalian Orthologs of Yeast Atg8. *Autophagy* **2017**, *13*, 834–853, doi:10.1080/15548627.2017.1287651.

48. Steinhilb, M.L.; Turner, R.S.; Gaut, J.R. The Protease Inhibitor, MG132, Blocks Maturation of the Amyloid Precursor Protein Swedish Mutant Preventing Cleavage by Beta-Secretase. *J Biol Chem* **2001**, *276*, 4476–4484, doi:10.1074/jbc.M008793200.

49. Harer, S.L.; Bhatia, M.S.; Bhatia, N.M. Proteasome Inhibitors Mechanism; Source for Design of Newer Therapeutic Agents. *J Antibiot* **2012**, *65*, 279–288, doi:10.1038/ja.2011.84.

50. Liu, P.-F.; Tsai, K.-L.; Hsu, C.-J.; Tsai, W.-L.; Cheng, J.-S.; Chang, H.-W.; Shiau, C.-W.; Goan, Y.-G.; Tseng, H.-H.; Wu, C.-H.; et al. Drug Repurposing Screening Identifies Tioconazole as an ATG4 Inhibitor That Suppresses Autophagy and Sensitizes Cancer Cells to Chemotherapy. *Theranostics* **2018**, *8*, 830–845, doi:10.7150/thno.22012.

51. Bosc, D.; Vezenkov, L.; Bortnik, S.; An, J.; Xu, J.; Choutka, C.; Hannigan, A.M.; Kovacic, S.; Loo, S.; Clark, P.G.K.; et al. A New Quinoline-Based Chemical Probe Inhibits the Autophagy-Related Cysteine Protease ATG4B. *Sci Rep* **2018**, *8*, 11653, doi:10.1038/s41598-018-29900-x.

52. Qiu, Z.; Kuhn, B.; Aebi, J.; Lin, X.; Ding, H.; Zhou, Z.; Xu, Z.; Xu, D.; Han, L.; Liu, C.; et al. Discovery of Fluoromethylketone-Based Peptidomimetics as Covalent ATG4B (Autophagin-1) Inhibitors Available online: https://pubs.acs.org/doi/pdf/10.1021/acsmedchemlett.6b00208 (accessed on 5 April 2022).

837   53. Chu, J.; Fu, Y.; Xu, J.; Zheng, X.; Gu, Q.; Luo, X.; Dai, Q.; Zhang, S.; Liu, P.; Hong, L.; et al. ATG4B
838   Inhibitor FMK-9a Induces Autophagy Independent on Its Enzyme Inhibition. *Arch Biochem Biophys*
839   **2018**, *644*, 29–36, doi:10.1016/j.abb.2018.03.001.

840   54. Akin, D.; Wang, S.K.; Habibzadegah-Tari, P.; Law, B.; Ostrov, D.; Li, M.; Yin, X.-M.; Kim, J.-S.;
841   Horenstein, N.; Dunn, W.A. A Novel ATG4B Antagonist Inhibits Autophagy and Has a Negative Impact
842   on Osteosarcoma Tumors. *Autophagy* **2014**, *10*, 2021–2035, doi:10.4161/auto.32229.

843   55. Nguyen, T.G.; Honson, N.S.; Arns, S.; Davis, T.L.; Dhe-Paganon, S.; Kovacic, S.; Kumar, N.S.; Pfeifer,
844   T.A.; Young, R.N. Development of Fluorescent Substrates and Assays for the Key Autophagy-Related
845   Cysteine Protease Enzyme, ATG4B. *Assay Drug Dev Technol* **2014**, *12*, 176–189,
846   doi:10.1089/adt.2013.561.

847   56. Kauffman, K.J.; Yu, S.; Jin, J.; Mugo, B.; Nguyen, N.; O'Brien, A.; Nag, S.; Lystad, A.H.; Melia, T.J.
848   Delipidation of Mammalian Atg8-Family Proteins by Each of the Four ATG4 Proteases. *Autophagy*
849   **2018**, *14*, 992–1010, doi:10.1080/15548627.2018.1437341.

850   57. Klionsky, D.J.; Abdel-Aziz, A.K.; Abdelfatah, S.; Abdellatif, M.; Abdoli, A.; Abel, S.; Abeliovich, H.;
851   Abildgaard, M.H.; Abudu, Y.P.; Acevedo-Arozena, A.; et al. Guidelines for the Use and Interpretation
852   of Assays for Monitoring Autophagy (4th Edition). *null* **2021**, 1–382,
853   doi:10.1080/15548627.2020.1797280.

854   58. Li, M.; Chen, X.; Ye, Q.-Z.; Vogt, A.; Yin, X.-M. A High-Throughput FRET-Based Assay for
855   Determination of Atg4 Activity. *Autophagy* **2012**, *8*, 401–412, doi:10.4161/auto.18777.

856   59. Scherz-Shouval, R.; Shvets, E.; Fass, E.; Shorer, H.; Gil, L.; Elazar, Z. Reactive Oxygen Species Are
857   Essential for Autophagy and Specifically Regulate the Activity of Atg4. *EMBO J* **2007**, *26*, 1749–1760,
858   doi:10.1038/sj.emboj.7601623.

859   60. Nguyen, N.; Olivas, T.J.; Mires, A.; Jin, J.; Yu, S.; Luan, L.; Nag, S.; Kauffman, K.J.; Melia, T.J. The
860   Insufficiency of ATG4A in Macroautophagy. *Journal of Biological Chemistry* **2020**, *295*, 13584–13600,
861   doi:10.1074/jbc.RA120.013897.

862   61. Xu, D.; Xu, Z.; Han, L.; Liu, C.; Zhou, Z.; Qiu, Z.; Lin, X.; Tang, G.; Shen, H.; Aebi, J.; et al.

863   Identification of New ATG4B Inhibitors Based on a Novel High-Throughput Screening Platform. *SLAS*

864   *Discov* **2017**, *22*, 338–347, doi:10.1177/1087057116639202.

865   62. Bertolin, G.; Sizaire, F.; Herbomel, G.; Reboutier, D.; Prigent, C.; Tramier, M. A FRET Biosensor

866   Reveals Spatiotemporal Activation and Functions of Aurora Kinase A in Living Cells. *Nat Commun*

867   **2016**, *7*, 12674, doi:10.1038/ncomms12674.

868   63. Cordelières, F.P.; Zhang, C. 3D Quantitative Colocalisation Analysis. In *Bioimage Data Analysis*

869   *Workflows*; Miura, K., Sladoje, N., Eds.; Learning Materials in Biosciences; Springer International

870   Publishing: Cham, 2020; pp. 33–66 ISBN 978-3-030-22386-1.

871   64. SMART Available online: https://smart.servier.com/ (accessed on 3 May 2022).

872

The LC3B FRET biosensor monitors the modes of action of ATG4B during autophagy in living cells

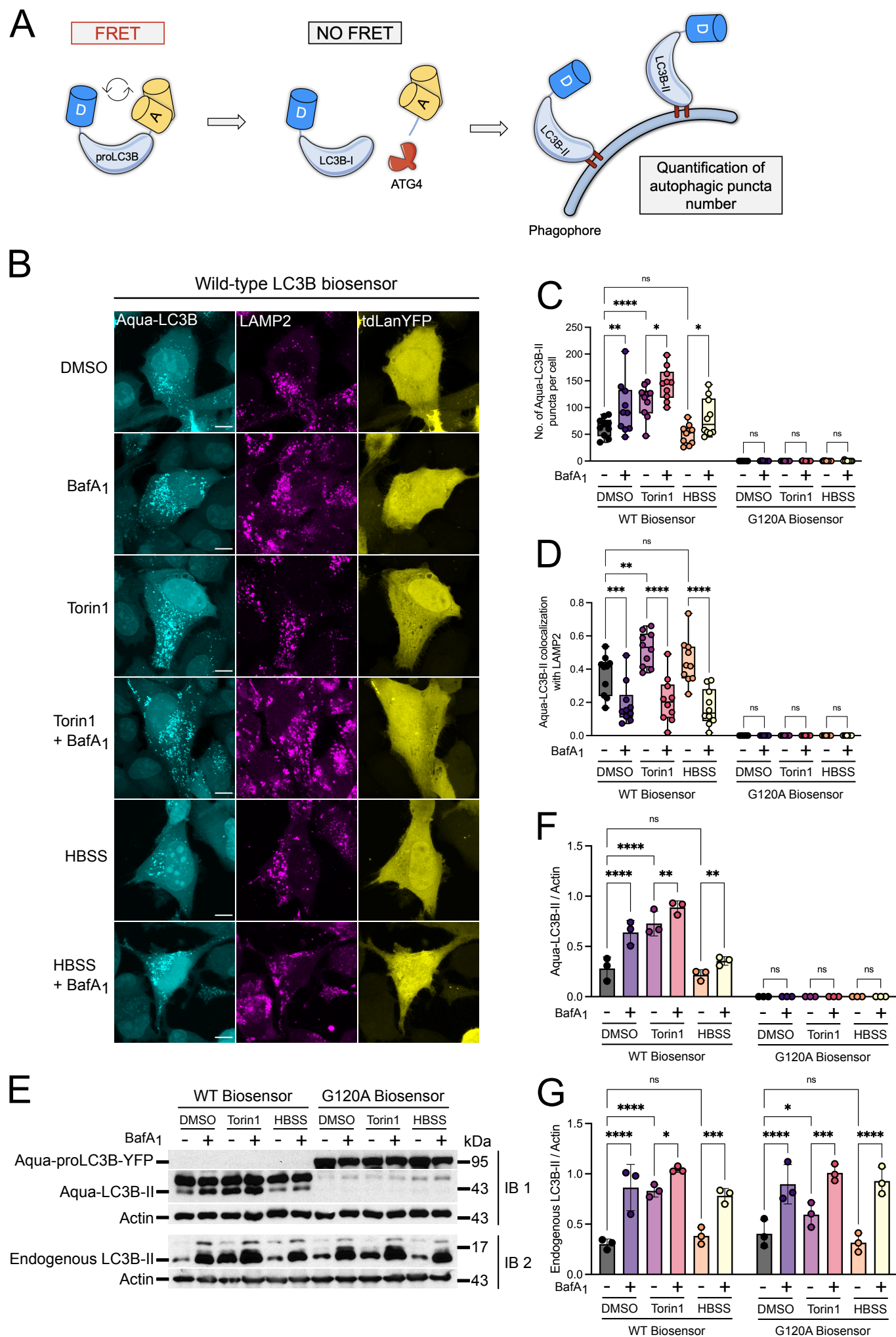**Elif Begüm Gökerküçük et al.**

Main figures

Figure 1

Figure 1. The LC3B biosensor reports on autophagy induction and/or lysosomal inhibition, and colocalizes with LAMP2 in an autophagy-dependent manner. (**A**) The cartoon illustrates the design and the mode of action of the LC3B biosensor. The biosensor was designed to flank the N- and C- termini of proLC3B with a donor (D, Aquamarine)-acceptor (A, tdLanYFP) FRET pair. When ATG4 is not active, the biosensor is expected to remain unprocessed in cells, allowing Aquamarine and tdLanYFP to perform FRET. Upon the proteolytic activity of ATG4, the biosensor is expected to be cleaved at its C-terminus, in turn losing its tdLanYFP moiety and the FRET effect with it. A successful priming of the biosensor is expected to yield Aquamarine-LC3B-I, which can then be integrated into the PE head groups of the phagophores and observed as puncta-shaped structures. The resulting Aquamarine-LC3B-II puncta-shaped structures can then be quantified to estimate the number of autophagosomes. (**B**) Representative fluorescence images of U2OS cells expressing the WT biosensor and stained for endogenous LAMP2. To investigate the changes in Aqua-LC3B puncta numbers and their colocalization with LAMP2, cells were treated with the following compounds: DMSO (6h), BafA$_1$ (6h, 100 nM), Torin1 (3h, 250 nM), Torin1 (3h, 250 nM) + BafA$_1$ (6h, 100 nM), HBSS (1h), HBSS (1h) + BafA1 (6h, 100 nM). Scale bar: 9 µm. (**C**) Quantification of the number of Aqua-LC3B-II puncta in cells expressing the WT or G120A biosensor and treated as indicated. (**D**) Quantification of the ratio of Aqua-LC3B-II puncta structures colocalizing with LAMP2-positive objects in cells expressing the WT or G120A biosensor and treated as indicated. n = 10 cells per condition from one representative experiment (of three) in (**C**) and (**D**). (**E**) Representative western blotting images and corresponding quantifications (**F, G**) of total lysates from U2OS cells expressing the WT or G120A biosensor and treated as indicated. IB1 and IB2 correspond to the same lysates blotted for overexpressed (IB1) or endogenous (IB2) LC3B forms. Loading control: Actin. n = 3 independent experiments *P < 0.05, **P < 0.01, ***P < 0.001, ****P < 0.0001, ns (not significant) as determined by two-way ANOVA with Tukey's multiple comparison test in (**C**) and (**D**), and with two-stage step-up method of Benjamini, Krieger and Yekutieli's multiple comparison test to control the false discovery rate in (**F**) and (**G**).
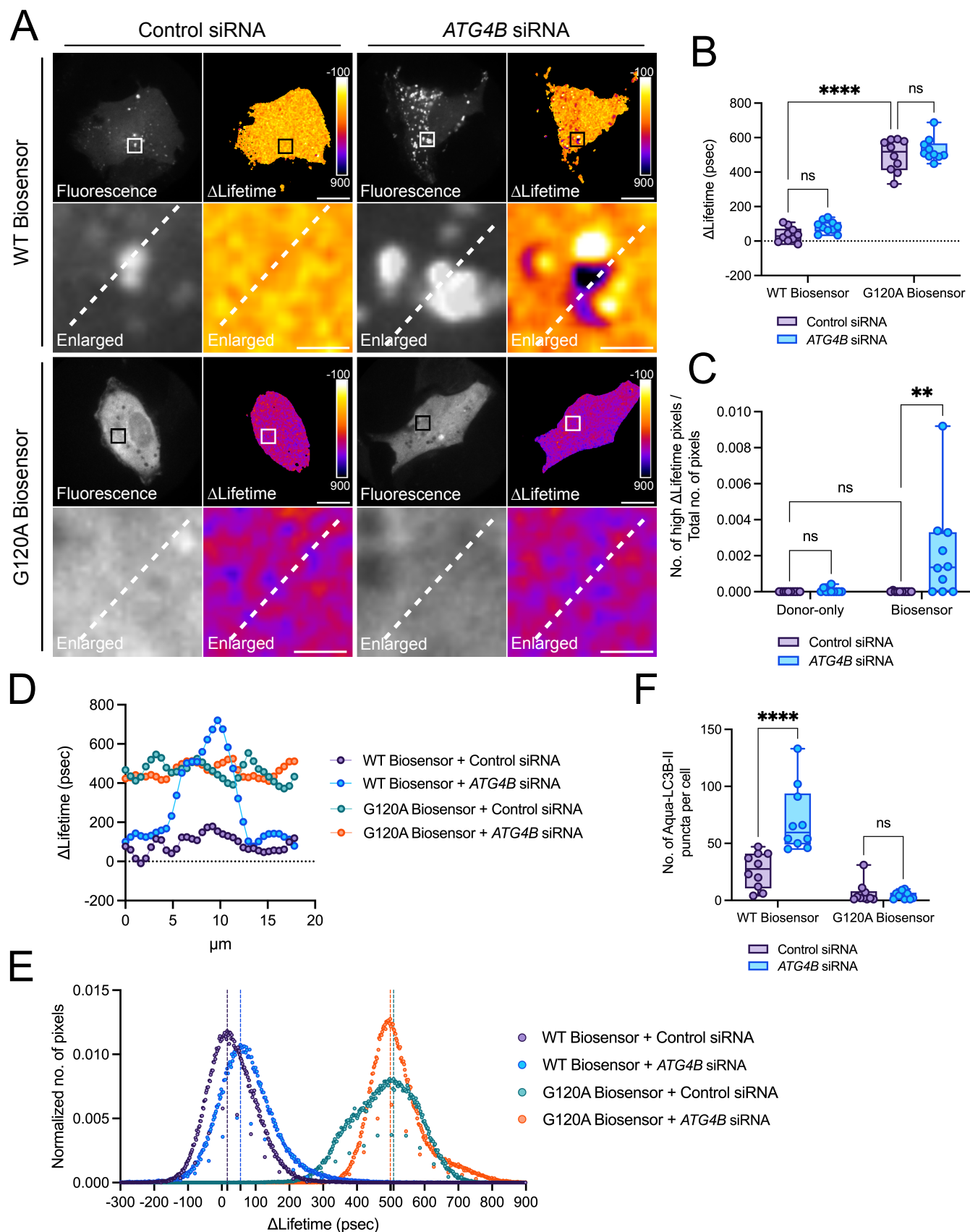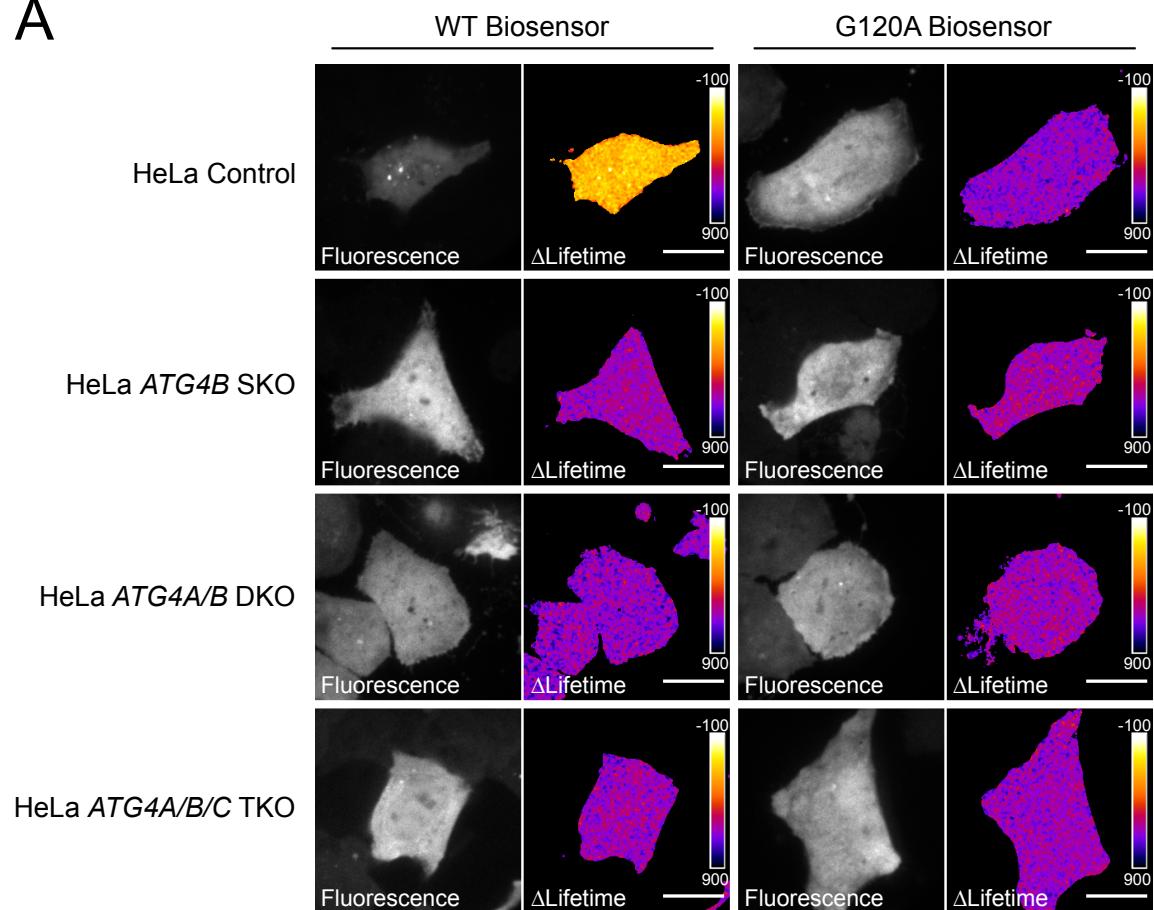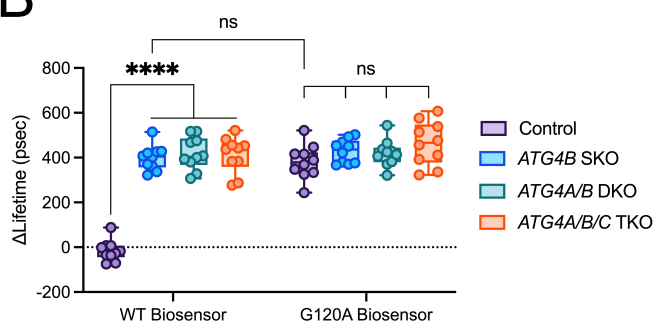
Figure 2

Figure 2. The knockdown of *ATG4B* lowers the priming of the LC3B biosensor. (**A**) Representative fluorescence and ΔLifetime images of U2OS cells co-expressing the WT or G120A biosensor with control or *ATG4B*-specific siRNAs, and analyzed by FRET/FLIM. Squares on the top images of WT or G120A biosensor panels illustrate the location of the enlarged images. Dotted lines on the enlarged images illustrate where the line analysis was performed. Pseudocolor scale: pixel-by-pixel ΔLifetime. Scale bars: overviews, 40 µm; enlarged, 6 µm. Mean ΔLifetime (**B**), number of high ΔLifetime pixels (**C**), line (**D**), histogram (**E**), and number of Aqua-LC3B-II puncta (**F**) analyses of U2OS cells co-expressing the WT or G120A biosensor with control or *ATG4B*-specific siRNAs in (**B**), (**D**), (**E**) and (**F**), and the WT donor or biosensor with control or *ATG4B* siRNA in (**C**). Vertical dotted lines on each histogram depicts the mode value in (**E**). n = 10 cells per condition from one representative experiment (of three) in (**B**), (**C**), (**E**) and (**F**). **P < 0.01, ****P < 0.0001, ns (not significant) as determined by two-way ANOVA with Tukey's multiple comparison test in (**B**), (**C**) and (**F**).
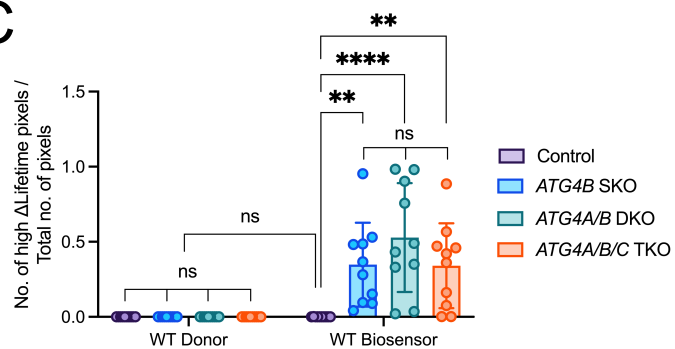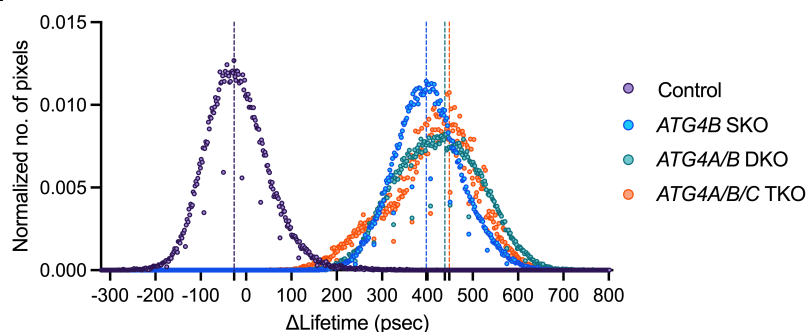
Figure 3

Figure 3. The absence of ATG4B maximizes the FRET response of the LC3B biosensor. (**A**) Representative fluorescence and ΔLifetime images of HeLa control, *ATG4B* SKO, *ATG4A/B* DKO, *ATG4A/B/C* TKO cells expressing the WT or G120A biosensor and analyzed by FRET/FLIM. Pseudocolor scale: pixel-by-pixel ΔLifetime. Scale bar: 40 μm. Mean ΔLifetime (**B**), number of high ΔLifetime pixels (**C**) and histogram (**D**) analyses of HeLa control, *ATG4B* SKO, *ATG4A/B* DKO, *ATG4A/B/C* TKO cells expressing the WT or G120A biosensor. The vertical dotted lines on each histogram depict the mode value in (**D**). n = 10 cells per condition from one representative experiment (of three) in (**B**), (**C**) and (**D**). $**P < 0.01$, $****P < 0.0001$, ns (not significant) as determined by two-way ANOVA with Tukey's multiple comparison test in (**B**) and (**C**).
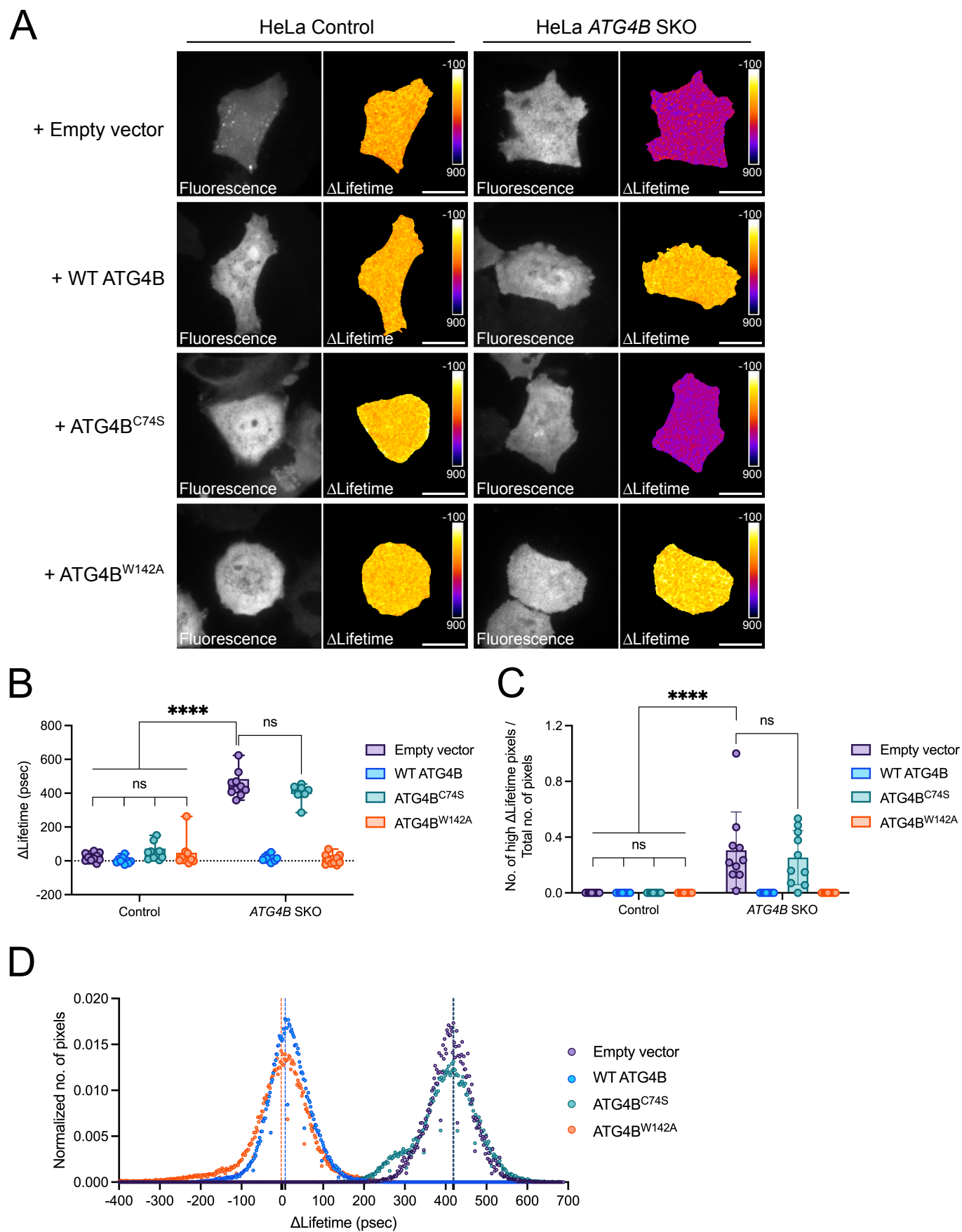
Figure 4

Figure 4. The priming deficiency of the LC3B biosensor is rescued when expressing WT or ATG4B^{W142A} in *ATG4B* **SKO cells.** (**A**) Representative fluorescence and ∆Lifetime images of control and *ATG4B* SKO HeLa cells co-expressing the WT biosensor with an empty vector, or with vectors expressing WT ATG4B, ATG4B^{C74S} or ATG4B^{W142A}, and analyzed by FRET/FLIM. Pseudocolor scale: pixel-by-pixel ∆Lifetime. Scale bar: 40 µm. Mean ∆Lifetime (**B**) and number of high ∆Lifetime pixels (**C**) analyses of control and *ATG4B* SKO cells co-expressing the WT biosensor with an empty vector, or with vectors expressing WT ATG4B, ATG4B^{C74S} or ATG4B^{W142A}. (**D**) The histogram analysis of *ATG4B* SKO cells co-expressing the WT biosensor with an empty vector, or with vectors expressing WT ATG4B, ATG4B^{C74S} or ATG4B^{W142A}. Vertical dotted lines on each histogram depict the mode value in (**D**). $n = 10$ cells per condition from one representative experiment (of three) in (**B**), (**C**) and (**D**). ****$P < 0.0001$, ns (not significant) as determined by two-way ANOVA with Tukey's multiple comparison test in (**B**) and (**C**).
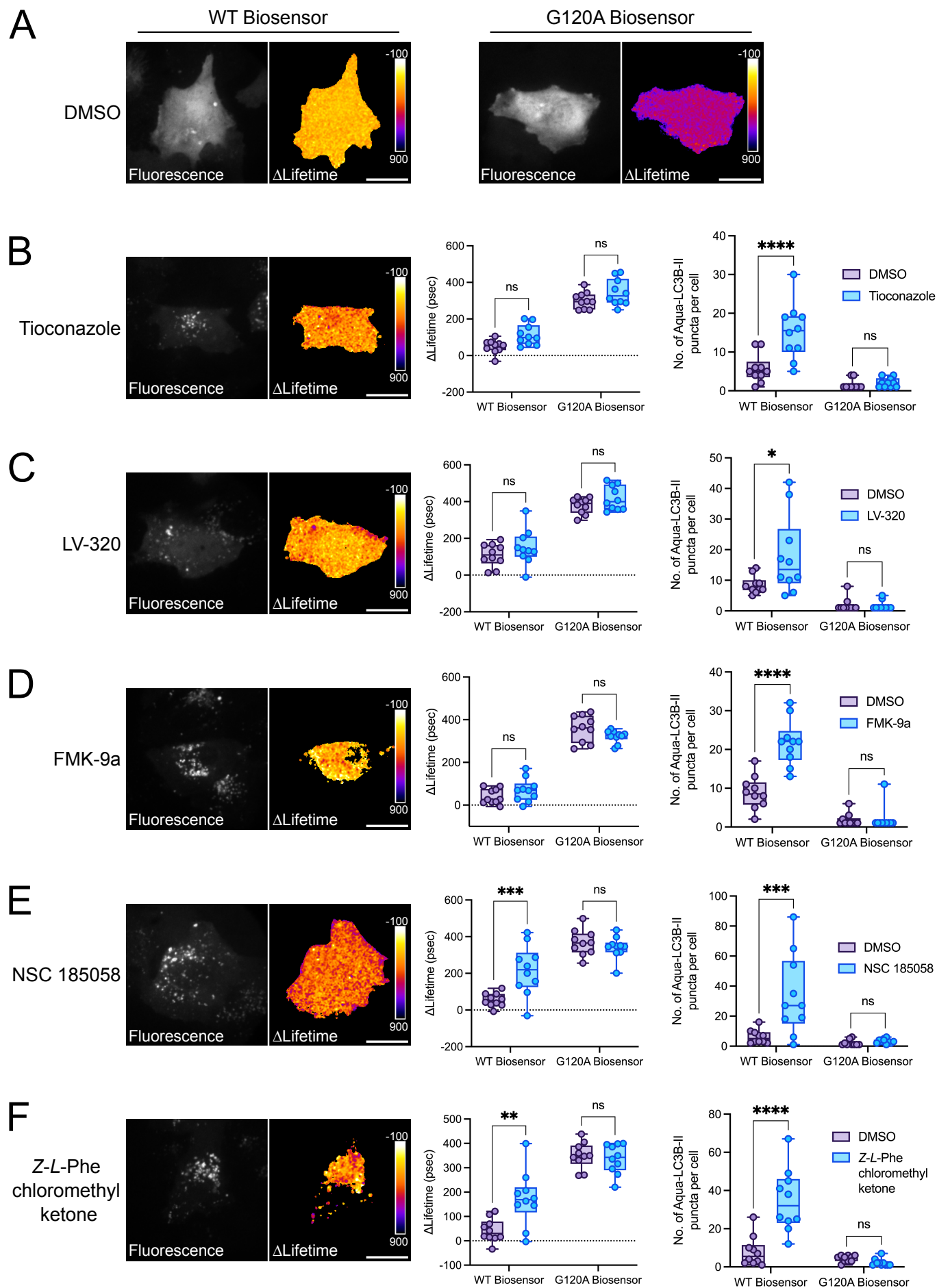
Figure 5

Figure 5. ATG4B inhibitors variably alter the ΔLifetime behavior and LC3B puncta number in cells expressing the LC3B biosensor. (**A**) Representative fluorescence and ΔLifetime images of HeLa cells expressing the WT or G120A biosensor, treated with DMSO (6h), and analyzed by FRET/FLIM. Representative fluorescence and ΔLifetime images of HeLa cells expressing the WT biosensor and treated with Tioconazole (6h, 4 µM) (**B**), LV-320 (6h, 120 µM) (**C**), FMK-9a (6h, 10 µM) (**D**), NSC 185058 (6h, 100 µM) (**E**), or *Z-L*-Phe chloromethyl ketone (6h, 3 µM) (**F**). Mean ΔLifetime and number of Aqua-LC3B-II puncta analyses of HeLa cells expressing the WT or G120A biosensor and treated with Tioconazole (6h, 4µM) (**B**), LV-320 (6h, 120 µM) (**C**), FMK-9a (6h, 10 µM) (**D**), NSC 185058 (6h, 100 µM) (**E**), or *Z-L*-Phe chloromethyl ketone (6h, 3 µM) (**F**). Pseudocolor scale: pixel-by-pixel ΔLifetime. Scale bars: 40 µm. *n* = 10 cells per condition from one representative experiment (of three) in (**B-F**). *$P < 0.05$, **$P < 0.01$, ***$P < 0.001$, ****$P < 0.0001$, ns (not significant) as determined by two-way ANOVA with Tukey's multiple comparison test in (**B-F**).
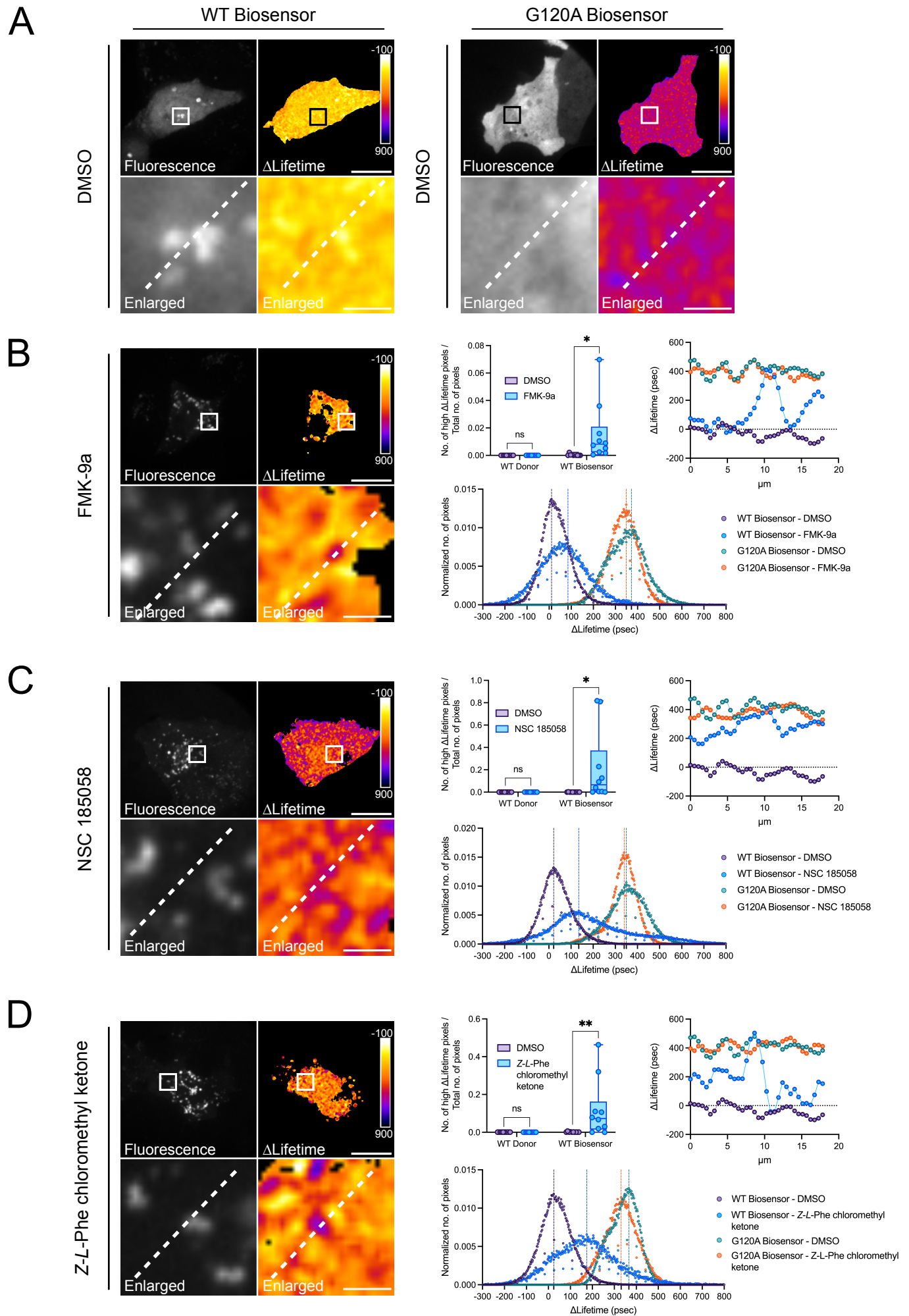
Figure 6

Figure 6. The LC3B biosensor reveals the mode of action of FMK-9a, NSC 185058 and *Z-L*-Phe chloromethyl ketone in cells. (**A**) Representative fluorescence and ∆Lifetime images of HeLa cells expressing the WT or G120A biosensor, treated with DMSO (6h), and analyzed by FRET/FLIM. Representative fluorescence and ∆Lifetime images of HeLa cells expressing the WT biosensor and treated with the following compounds: FMK-9a (6h, 10 µM) (**B**), NSC 185058 (6h, 100 µM) (**C**), or *Z-L*-Phe chloromethyl ketone (6h, 3 µM) (**D**). Squares on the top images of WT or G120A biosensor panels illustrate the location of the enlarged images. Dotted lines on the enlarged images illustrate where the line analysis was performed. Pseudocolor scale: pixel-by-pixel ∆Lifetime. Scale bars: overviews, 40 µm; enlarged, 6 µm. Number of high ∆Lifetime pixels analysis of HeLa cells expressing the WT donor or biosensor and treated with FMK-9a (6h, 10 µM) (**B**), NSC 185058 (6h, 100 µM) (**C**), or *Z-L*-Phe chloromethyl ketone (6h, 3 µM) (**D**). Line and histogram analyses of HeLa cells expressing the WT or G120A biosensor and treated with FMK-9a (6h, 10 µM) (**B**), NSC 185058 (6h, 100 µM) (**C**), or *Z-L*-Phe chloromethyl ketone (6h, 3 µM) (**D**). $n = 10$ cells per condition from one representative experiment (of three) in (**B**-**D**). *$P < 0.05$, **$P < 0.01$, ns (not significant) as determined by two-way ANOVA with Tukey's multiple comparison test in (**B**-**D**).